ISSN 2444-4987

Journal of Research and Development

Volume 9 Issue 23 – January – June – 2023

ECORFAN®

Journal of Research and Development, Volume 9, Issue 23, June - 2023, is a sixmonthly Journal edited by ECORFAN-Spain. Matacerquillas Street 38, CP: 28411. Moralzarzal - Madrid. WEB: http://www.ecorfan.org/spain/rj_investigacion_d.php, revista@ecorfan.org. Editor in Chief: VARGAS-DELGADO, Oscar. PhD. ISSN 2444-4987. Responsible for the last update of this issue ECORFAN Computer Unit. Escamilla Bouchán-Imelda, Luna Soto-Vladimir, updated to June 30, 2023.

Journal of Research and Development

Definition of Journal

Scientific Objectives

Support the international scientific community in its written production Science, Technology and Innovation in the Field of Humanities and Behavioral Sciences, in Subdisciplines of industrial development, project model, computer application, research production, systems development, research networks, application design, programming and development proposals.

ECORFAN-Mexico, S.C. is a Scientific and Technological Company in contribution to the Human Resource training focused on the continuity in the critical analysis of International Research and is attached to CONAHCYT-RENIECYT number 1702902, its commitment is to disseminate research and contributions of the International Scientific Community, academic institutions, agencies and entities of the public and private sectors and contribute to the linking of researchers who carry out scientific activities, technological developments and training of specialized human resources with governments, companies and social organizations.

Encourage the interlocution of the International Scientific Community with other Study Centers in Mexico and abroad and promote a wide incorporation of academics, specialists and researchers to the publication in Science Structures of Autonomous Universities - State Public Universities - Federal IES - Polytechnic Universities - Technological Universities - Federal Technological Institutes - Normal Schools - Decentralized Technological Institutes - Intercultural Universities - S & T Councils - CONAHCYT Research Centers.

Scope, Coverage and Audience

Journal of Research and Development is a Journal edited by ECORFAN-Mexico S.C in its Holding with repository in Spain, is a scientific publication arbitrated and indexed with semester periods. It supports a wide range of contents that are evaluated by academic peers by the Double-Blind method, around subjects related to the theory and practice of industrial development, project model, computer application, research production, systems development, research networks, application design, programming and development proposals with diverse approaches and perspectives , That contribute to the diffusion of the development of Science Technology and Innovation that allow the arguments related to the decision making and influence in the formulation of international policies in the Field of Humanities and Behavioral Sciences. The editorial horizon of ECORFAN-Mexico® extends beyond the academy and integrates other segments of research and analysis outside the scope, as long as they meet the requirements of rigorous argumentative and scientific, as well as addressing issues of general and current interest of the International Scientific Society.

Editorial Board

Arbitration Committee

MEDA - LARA, Rosa Martha. PhD
Universidad de Guadalajara

FIGUEROA - DÍAZ, María Elena. PhD
Universidad Nacional Autónoma de México

GARCÍA - Y BARRAGÁN, Luis Felipe. PhD
Universidad Nacional Autónoma de México

CORTÉS, María de Lourdes Andrea. PhD
Instituto Tecnológico Superior de Juan Rodríguez

VILLALOBOS - ALONZO, María de los Ángeles. PhD
Universidad Popular Autónoma del Estado de Puebla

ROMÁN - KALISCH, Manuel Arturo. PhD
Universidad Nacional Autónoma de México

CHAVEZ - GONZALEZ, Guadalupe. PhD
Universidad Autónoma de Nuevo León

GARCÍA - VILLANUEVA, Jorge. PhD
Universidad Nacional Autónoma de México

DE LA MORA - ESPINOSA, Rosa Imelda. PhD
Universidad Autónoma de Querétaro

PADILLA - CASTRO, Laura. PhD
Universidad Autónoma del Estado de Morelos

DELGADO - CAMPOS, Genaro Javier. PhD
Universidad Nacional Autónoma de México

Assignment of Rights

The sending of an Article to Journal of Research and Development emanates the commitment of the author not to submit it simultaneously to the consideration of other series publications for it must complement the Originality Format for its Article.

The authors sign the Authorization Format for their Article to be disseminated by means that ECORFAN-Mexico, S.C. In its Holding Spain considers pertinent for disclosure and diffusion of its Article its Rights of Work.

Declaration of Authorship

Indicate the Name of Author and Coauthors at most in the participation of the Article and indicate in extensive the Institutional Affiliation indicating the Department.

Identify the Name of Author and Coauthors at most with the CVU Scholarship Number-PNPC or SNI-CONAHCYT- Indicating the Researcher Level and their Google Scholar Profile to verify their Citation Level and H index.

Identify the Name of Author and Coauthors at most in the Science and Technology Profiles widely accepted by the International Scientific Community ORC ID - Researcher ID Thomson - arXiv Author ID - PubMed Author ID - Open ID respectively.

Indicate the contact for correspondence to the Author (Mail and Telephone) and indicate the Researcher who contributes as the first Author of the Article.

Plagiarism Detection

All Articles will be tested by plagiarism software PLAGSCAN if a plagiarism level is detected Positive will not be sent to arbitration and will be rescinded of the reception of the Article notifying the Authors responsible, claiming that academic plagiarism is criminalized in the Penal Code.

Arbitration Process

All Articles will be evaluated by academic peers by the Double Blind method, the Arbitration Approval is a requirement for the Editorial Board to make a final decision that will be final in all cases. MARVID® is a derivative brand of ECORFAN® specialized in providing the expert evaluators all of them with Doctorate degree and distinction of International Researchers in the respective Councils of Science and Technology the counterpart of CONAHCYT for the chapters of America-Europe-Asia- Africa and Oceania. The identification of the authorship should only appear on a first removable page, in order to ensure that the Arbitration process is anonymous and covers the following stages: Identification of the Journal with its author occupation rate - Identification of Authors and Coauthors - Detection of plagiarism PLAGSCAN - Review of Formats of Authorization and Originality-Allocation to the Editorial Board- Allocation of the pair of Expert Arbitrators-Notification of Arbitration -Declaration of observations to the Author-Verification of Article Modified for Editing-Publication.

Instructions for Scientific, Technological and Innovation Publication

Knowledge Area

The works must be unpublished and refer to topics of industrial development, project model, computer application, research production, systems development, research networks, application design, programming and development proposals and other topics related to Humanities and Behavioral Sciences.

Presentation of the Content

In the first article we present, *Numerical modeling of the behavior of a lithium battery after a collision*, by FLORES-LÓPEZ, Holbein Eli, LÓPEZ-GARCÍA, Claudio and SANTIAGO-AMAYA, Jorge, with ascription in the Instituto Politécnico Nacional, as the next article we present, *Use of a smartwatch for home blood pressure measurement*, by MEX-ÁLVAREZ, Rafael Manuel de Jesús, GUILLEN-MORALES, María Magali, YANEZ-NAVA, David and NOVELO-PÉREZ, María Isabel, with ascription in the, Instituto Tecnológico de Ciudad Madero, as the next article we present, *Strain localization instability in seafloor spreading centers of the Carmen Basin, southern Gulf of California*, by JULIÁ-MIRALLES, Marc, YARBUH, Ismael, SPELZ, Ronald M. and NEGRETE-ARANDA, Raquel, with ascription in the Universidad Autónoma de Baja California, as the last article we present, *Design of a two-stage air monitoring and filtration system for implementation in enclosed spaces*, by HERNÁNDEZ-SÁNCHEZ, Uriel Alejandro, VÁZQUEZ-ROSAS, Sergio, CABALLERO-LÓPEZ, Emma Isabel and FLORES-SÁNCHEZ, Verónica, with ascription in the Universidad Tecnológica del Centro de Veracruz.

Content

Article **Journal of Research and Development**
June 2023, Vol.9 No.23 1-9

Numerical modeling of the behavior of a lithium battery after a collision

Modelado numérico del comportamiento de una batería de litio tras colisión

FLORES-LÓPEZ, Holbein Eli†*, LÓPEZ-GARCÍA, Claudio and SANTIAGO-AMAYA, Jorge

Instituto Politécnico Nacional, Escuela Superior de Ingeniería Mecánica y Eléctrica Unidad Zacatenco. Maestría en Ciencias en Ingeniería Mecánica, C.P. 07738 Ciudad de México, México.

ID 1st Author: *Holbein Eli, Flores-López* / **ORC ID:** 0009-0007-8793-7021 **CVU CONAHCYT ID:** 1141571

ID 1st Co-author: *Claudio, López-García* / **ORC ID:** 0000-0002-8361-8249 **CVU CONAHCYT ID:** 333862

ID 2nd Co-author: *Jorge, Santiago-Amaya* / **ORC ID:** 0000-0003-3432-4305, **CVU CONHACYT ID:** 490214

DOI: 10.35429/JRD.2023.23.9.1.9 Received: January 10, 2023; Accepted: June 30, 2023

Abstract

This study is carried out to verify numerically the deformation and Von Misses stresses of a lithium-Ion battery (Li6PF 43 ah, 3.7v) after impact against a solid sphere, using the specialized program in Dynamic Simulation. and Ls-Dyna Finite Elements. With the aim of advancing in the studies to validate the safety of batteries in electric cars this study creates a model of the analyzed prismatic battery.

Battery, Finite element, Lithium, Simulation

Resumen

Se realiza este estudio con el fin de comprobar numéricamente la deformación y los esfuerzos de Von Misses de una batería de Ion de litio, (Li6PF 43 ah, 3.7v) tras el impacto contra una esfera sólida, haciendo uso del programa especializado en Simulación Dinámica y Elementos Finitos Ls-Dyna. Con el objetivo de avanzar en los estudios para validar la seguridad de baterías en automóviles eléctricos, este estudio crea un modelo propio de la batería prismática analizada.

Batería, Elementos finitos, Litio, Simulación

Citation: FLORES-LÓPEZ, Holbein Eli, LÓPEZ-GARCÍA, Claudio and SANTIAGO-AMAYA, Jorge. Numerical modeling of the behavior of a lithium battery after a collision. Journal of Research and Development. 2023. 9-23:1-9.

* Author's Correspondence (E-mail: holbeineli@gmail.com)
† Researcher contributing as first author.

Introduction

With the advent of lithium-ion battery technology, hybrid or fully electric cars have become popular on the world's roads. With the advent of this type of transport, new safety protocols had to be implemented in case of serious accidents (Electric Cars Are Triggering New Emergency Protocols Due to Batteries and Their Fire Hazards, n.d.; NFPA, n.d.).

Cases of accidents involving problems with electric vehicle batteries have been reported (Beauregard et al., 2008)(U.S. Department of Transportation, 2012)(Feng et al., 2018). These are caused by several reasons, one of which is mechanical abuse, which includes deformation and displacements, caused by forces applied during a collision, which would result in battery pack deformation, separator rupture causing short circuits and leakage of flammable electrolyte (Feng et al., 2018).

With existing technology, aspects of vehicle safety can be analysed, such as software simulation, where the behaviour of a battery bank can be analysed after a sudden impact and under specific circumstances.

In a study conducted at the Department of Mechanical Engineering at Ningb University of Technology in China (Chen et al., 2020), a solid sphere is impacted on a lithium battery, resulting in stresses and a marked footprint on the battery. The data obtained are corroborated by performing a numerical analysis using the finite element program Ls-Dyna, by running a simulation to observe the Von Misses stresses, in such a way that it contributes to express results in a numerical way.

Distortion energy

The strain energy of an element is the increase in energy associated with the deformation of the element. During a tensile test, the elongation of a specimen under the action of an increasing load is measured, work is expended and this work is partially or totally transformed into potential strain energy. If the deformation does not reach the elastic limit, the work done by the external force is completely transformed into potential energy and can be recovered by gradually unloading the deformed bar (STEPHEN P. TIMOSHENKO, 1972).

The strain energy density of a material is the strain energy per unit volume, which is equal to the area under the stress-strain curve.

$$U = \int_0^{x_1} P dx \tag{1}$$

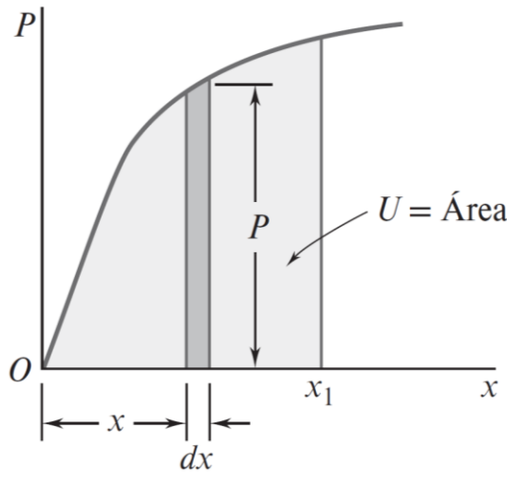

Figure 1 Stress-Strain graph

Strain energy can be used to determine the effects of impact loads on structures or machine components. For practical purposes, equations 2 and 3 are given, in which the strain energy as a function of geometric, elastic and load characteristics, and in another is expressed as a function of the same characteristics and the elongation, respectively.

$$U = \frac{Pl}{AE} \tag{2}$$

$$U = \frac{Pl}{AE} \tag{3}$$

The theory states that: "Failure will occur when the distortion energy per unit volume due to the absolute maximum stresses at the critical point is equal to or greater than the distortion energy per unit volume of a specimen in the tensile test at the time of creep" (FERDINAND P. BEER, 2015).

This criterion determines the distortion energy in a material, which is the energy associated with changes in the shape of the material. It is also known as the Von Mises criterion. A component is safe as long as the maximum value of the distortion energy per unit volume in that material remains smaller than the distortion energy per unit volume required to yield a specimen of the same material under stress.

The equivalent stress is given by:

ISSN-On line: 2444-4987

$$\sigma_{eq} = \sqrt{\frac{1}{2}[(\sigma_1 - \sigma_2)^2 + (\sigma_2 - \sigma_3)^2 + (\sigma_3 - \sigma_1)^2]} \quad (4)$$

Comparing the graph given by Von Misses against that of Tresca, the Von Misses graph being the ellipse and the Tresca graph being the hexagon formed; it establishes the allowable stress values to achieve design reliability of materials.

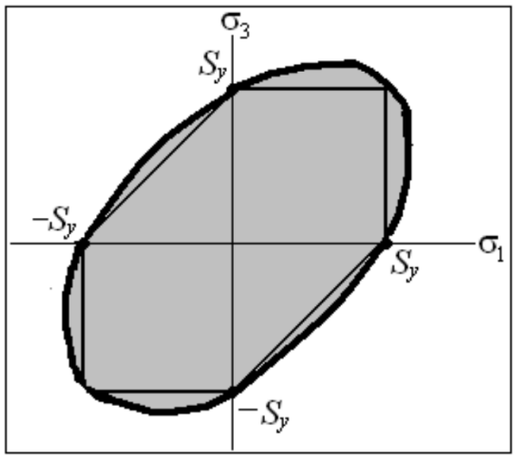

Figure 2 Von Misses vs Tresca chart

Ls-Dyna

Ls-Dyna is a multiphysics simulation program capable of simulating complex problems. It uses a general finite element code for the extensive analysis of static and dynamic deformations of structures, including fluid-coupled structures. The main solution methodology used by this application is based on an explicit integration time. A contact-impact algorithm allows difficult contact problems to be easily treated with heat transfer including interface contact.

Ls-Dyna currently contains approximately 1000 constitutive models and 10 equations to cover a wide range of material behaviour.

Originated at Lawrence Livermore National Laboratory, the first application was for the analysis of stresses in structures subjected to various impact loads. The application required certain computational resources, and the need for a much faster version was necessary, as the results took a long time to appear, all in accordance with the technology at the time.

It is widely used in the automotive industry for the design and development of projects involving the improvement and safety of its occupants, as well as in the study of metal deformation. On the other hand, in the aerospace industry it is used in the study of materials and the prevention of structural errors in new designs. It is also being used for non-linear materials that do not exhibit ideally elastic behaviour.

It consists of a single executable file and uses line-driven commands. Therefore, all that is required to run Ls-Dyna is a command console, the executable, an input file and enough free disk space to run the calculation. All input files are in ASCII format, although it can run various types of files dealing with CAD design (STL) and can therefore be prepared using any text editor. Input files can also be prepared with the help of a graphics preprocessor.

Ls-Dyna is one of the most popular Code-based explicit finite element solvers used for structural simulation when subjected to dynamic loads. The program is used in industry for the design and prediction of various structures ranging from automobiles to aircraft components when subjected to shock or impact loads (JOHN O. HALLQUIST, 2006).

Battery design

Li-ion batteries have a high energy density, good high temperature performance and are recyclable. The main advantages of Li-ion batteries are low memory effect, high specific power (W/kg), high specific energy (Wh/kg) and long life. These characteristics make these batteries suitable for use in hybrid electric vehicles and electric vehicles (Iglesias et al., 2012).

On the downside, due to the nature of the chemical reactions of lithium, these batteries are not tolerant of overcharging or over-discharging and can easily be damaged if the control strategy is inadequate, making safety an added issue. Commercial Li-ion batteries often have protection systems built into the battery body itself to limit charging voltages, discharge voltages and disconnect cells from the load in the event of overcurrent or overtemperature (Wang et al., 2019).

ISSN-On line: 2444-4987

Impact testing

Zhang developed a finite element model, a battery separator in Ls-Dyna. Based on uniaxial tensile and full-thickness compression test data. The model allowed to obtain the response of the separator under drilling tests with different drill head sizes. The model also correctly responded to the effect of anisotropic material on the shape and curvature of the deformation in two planes of anisotropy figure 3 (Zhang *et al*., 2016).

Figure 3 Indentation with different sphere sizes

Meng L. performed a nail penetration test to observe the behaviour of a lithium battery. The cell chosen is a commercial hard-shell prismatic lithium-ion cell with a rated capacity of 202 Ah. The test was performed with the lithium cell encapsulated with a silicon base, inside a thick-walled metal enclosure. The encapsulation technique was devised and designed to ensure that, once the cell is vented, the encapsulation at the vent perimeter would also break down without damaging the adjacent encapsulation. Figure 4 shows the nail penetration test to the metal enclosure containing the silicon-encapsulated battery and a general schematic of the test.

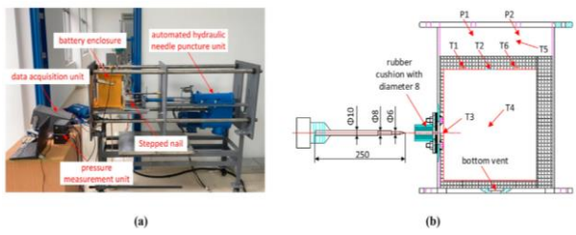

Figure 4 a) penetration test set up. b) penetration test schematic

A second penetration test was performed, only this time more batteries connected in series were used. What happened this time was that the efficiency of encapsulating the batteries with silicone is tested, since, in case of leakage, the silicone material keeps the other batteries and their terminals isolated (Meng et al., 2022). From the studies with the encapsulation method, Lingyu recorded data showing that the technique really works to dissipate heat, figure 5.

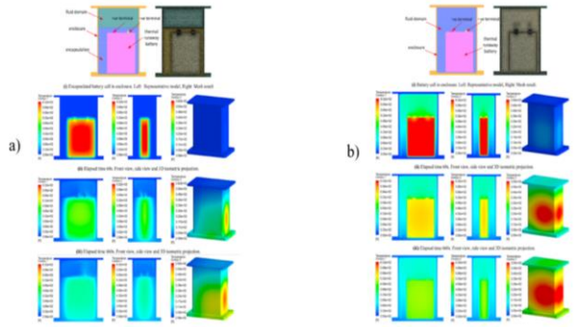

Figure 5 a) Temperature distribution with the encapsulation technique. b) Temperature distribution without encapsulation

Another research paper, Lars Greve and Clemens Fehrenbach, discuss the safety of lithium-ion battery cells, and talk about two general strategies that can be applied to safety; the first is to improve safety by avoiding overuse and protecting the cells adequately; the second is to improve cell safety by understanding the mechanisms that cause internal short circuits under mechanical load and improving cells or cell components accordingly. In their study they perform mechanical tests with cylindrical lithium-ion cells. The simulation model allows the representation of cell deformation and a tensile-based fracture criterion to predict the state of charge and the location of internal short-circuit initiation during deformation. I conducted quasi-static tests, which showed that the cells could withstand significant deformation before a short circuit could occur (Greve & Fehrenbach, 2012).

With a force of less than .2 KN. A punch velocity of .5 mm/ms and an actual test velocity of .1 mm/s it is proposed as future work to involve experimental characterisation and numerical simulation of the individual components of the gelatin roll (anode, separator and cathode) and their interaction during mechanical loading. [9]

Karen Dai, He Zhang and Zheng You used the machete hammer test, which converts the kinetic energy of a hammer's counterweight into gravitational potential energy. They performed impact tests on a lithium-ion battery. During the tests they monitored the voltage behaviour of the battery. The results obtained show a significant change in voltage during impact. Another result was to measure internally the deceleration at the time of an embedding, by means of the oscillation at the time of vibration caused by the generated stress waves.

ISSN-On line: 2444-4987

The impact circuit model presented in this paper can analyse the failure behaviour under high-speed impact, but cannot reveal structural parameters of lithium-ion batteries in impact resistance. They propose an increase of separator thickness which significantly improves the failure phenomenon of lithium-ion batteries under high impact (Yu et al., 2021).

Methodology

For this work, the case study of a prismatic battery indentation from a thesis study (Chen et al., 2020) will be replicated numerically. This experiment consists of a drop-weight impact test system (model: DHR-1808) to impact a prismatic battery. A spherical indenter was used. The impact velocity was varied from 1.5 m/s to 4.5 m/s increasing by .25 to .25 and .5 m/s. A total of 8 indentations were performed. What will be reproduced is only the moment of impact to the battery, without taking into account the test machine, only the battery and the indenter.

With the data provided, we proceeded with the numerical simulation replica using the Ls-Dyna programme for the battery impact test. The steps necessary to arrive at the final result will be explained, and from this we will compare the data obtained with the experiment of the thesis on which this work is based.

Block diagram of the methodology

BLOCK 1
The battery was disassembled to examine its internal components and obtain the necessary measurements to recreate its CAD model.

↓

BLOCK 2
With the measurements obtained of the internal components of the battery, we proceeded to draw and recreate each essential part of the battery in CAD.

↓

BLOCK 3
With the 3 essential parts of the battery an assembly was made to obtain the CAD model of the battery.

↓

BLOCK 4
The CAD model was saved in IGES format and opened in the dynamic simulation program Ls-Dyna.

↓

BLOCK 5
The Ls-Dyna program cards were programmed with the necessary boundary conditions and the essential materials to recreate the moment of impact of the battery with the half-sphere indenter and observe if the behaviour of the battery is the same, similar or different to the experimental case study being evaluated in this work.

↓

BLOCK 6
With the Ls-Dyna cards correctly programmed, we proceeded to run the simulation.

The following figure shows the finished CAD model, the design program used was SolidWorks.

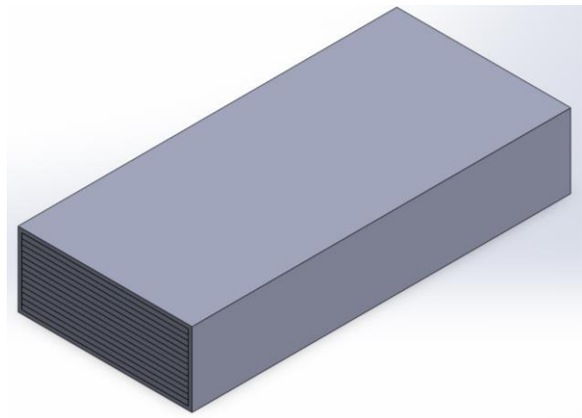

Figure 6

Once the CAD model design step was completed, the next step was to use the Ls-Dyna program for the simulation of the battery impact. The SolidWorks file with extension .igs was used and loaded into the Ls-Dyna program. The following figure shows all the components ready and meshed for simulation.

ISSN-On line: 2444-4987

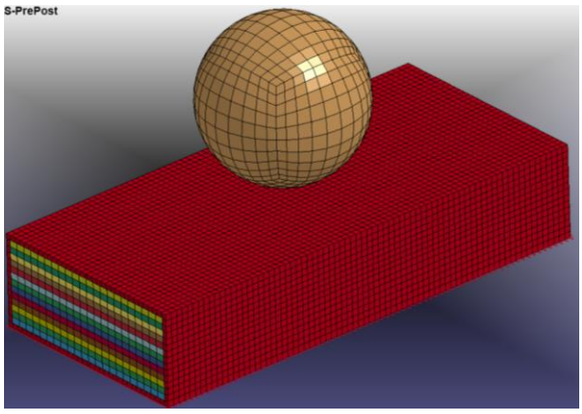

Figure 7

As can be seen in the figure, the model was trimmed at the ends to optimise and reduce computational costs. It is considered that the results do not vary much due to the eliminated parts of the rounded edges.

The cards that were used for preprocessing and simulation are presented below.

First, the materials were added with their corresponding densities, Young's modulus, Poisson's ratio and yield stress.

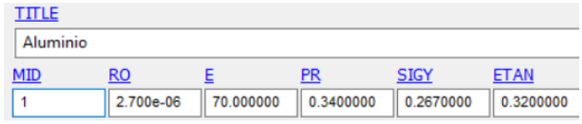

Figure 8 Mat 003 Plastic Kinematic (Aluminum)

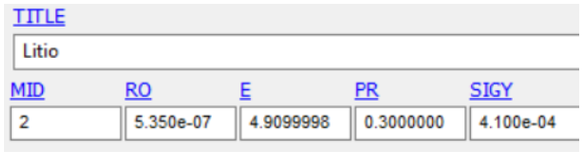

Figure 9 Mat 003 Plastic Kinematic (Litio)

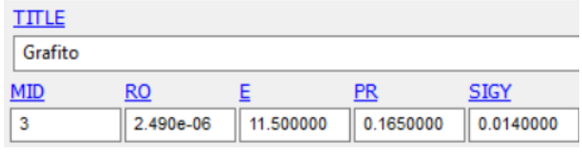

Figure 10 Mat 003 Plastic Kinematic (Graphite)

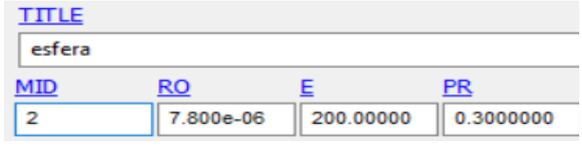

Figure 11 Mat 020 Rigid, material for the sphere (Steel)

Then 2 sections are created, one for each type of solid that integrates the model. The battery casing will be taken as a Shell, as this is the mesh that was assigned to it by the program tools. For the sphere and the other parts of the battery, it will be taken as a Solid, since the programme tools allowed a solid mesh for these parts.

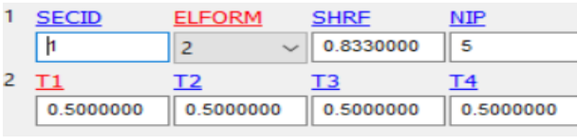

Figure 12 Shell section with a thickness of .5 mm

Figure 13 Solid Section, the card is created without adding anything

The next step is to create a Part to assign a material and a section to each Part in the simulation, in this case we have 15 parts to which we need to add a material and a section.

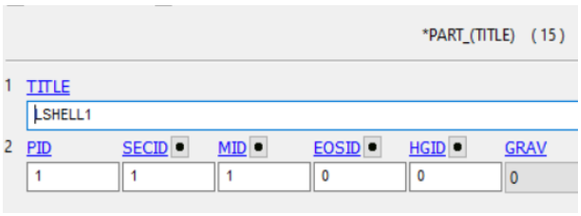

Figure 14 Part 1 with SECID as section and MID as material

For each component a section and material needs to be assigned as appropriate, for this case components 2 to 15 will be assigned a Solid section corresponding to their mesh type and the housing will be assigned a Shell section due to its assigned mesh type. The sphere will be assigned to the steel material and the shell to aluminium, all others will be sandwiched between graphite and lithium.

We assign a negative velocity on the y-axis to the sphere.

Figure 15 In NSID/PID select the desired item to be assigned a speed

ISSN-On line: 2444-4987

A motion constraint is programmed to make the battery stand still, simulating the test table where it is located, using the SPC_SET board, as shown in Figure 17.

Figure 17 The section of nodes created is chosen

When it comes to choosing a node section, it will ask us to create it, so we create it on the entire bottom side, as shown in Figure 17.

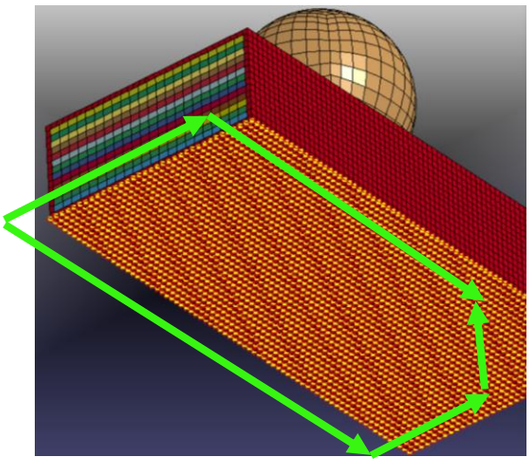

Figure 18 Movement restriction using SET_NODE (marked with green colour)

We continue with filling the cards of the types of contacts that will occur in the simulation. Taking into account that the sphere is the master and where it hits is the slave, we fill the fields with the necessary parts. After the first contact of the sphere against the first layer of the battery, the same logic is followed to determine who is now the master and who is the slave. As shown in Figures 18-32.

Figure 19 Contact1

Figure 20 Contact 2

Figure 21 Contact 3

Figure 22 Contact 4

Figure 23 Contact 5

Figure 24 Contact 6

Figure 25 Contact 7

Figure 26 Contact 8

Figure 27 Contact 9

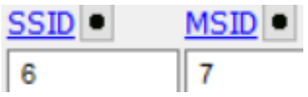

Figure 28 Contact 10

Figure 29 Contact 11

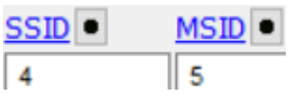

Figure 30 Contact 12

Figure 31 Contact 13

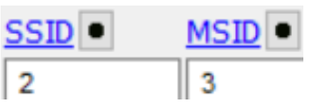

Figure 32 Contact 14

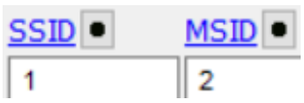

Figure 33 Contact 15

Finally, we set the time we want the simulation to last, we do it at 1 ms Figure 33.

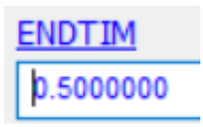

Figure 34 Control_Termination card

We must also give a time in which we want the program to make measurements of the results, and we will set it to .01, Figure 34.

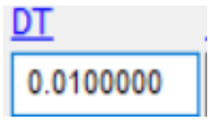

Figure 35 Binary D3plot card

We save our .k file and solve it with the Ls-Dyna solver, when finished we can open the D3plot file that it generates and that is the file to visualize the results.

We also achieve what we expected, to reduce the computational costs with the simplification of the design, as previously explained in Figure 35.

```
estimated total cpu time          =      2250 sec
estimated cpu time to complete    =      2248 sec
estimated total clock time        =      3426 sec
estimated clock time to complete  =      3424 sec
```

Figure 36 Simulation times

Results

Table III.3 shows the results of the simulation with a sphere velocity of 2 m/s. Table 1 shows a comparison of the experimentally obtained results against the simulation results in Ls-Dyna.

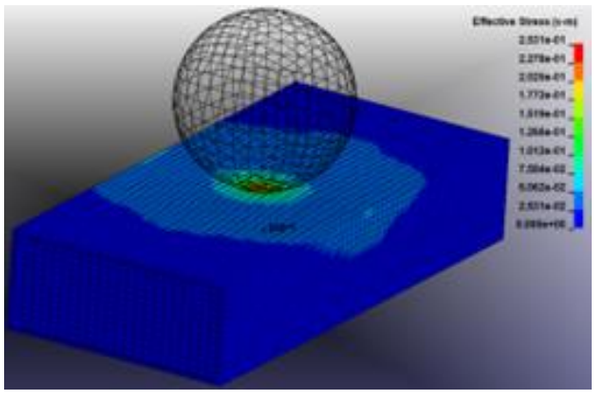

Figure 37 Battery impact zone: Time: 1.9998 m/s Von Misses Maximum Stress = .2531 Pa

Time: 1.9998 m/s Von Misses Maximum Stress =.2531Pa

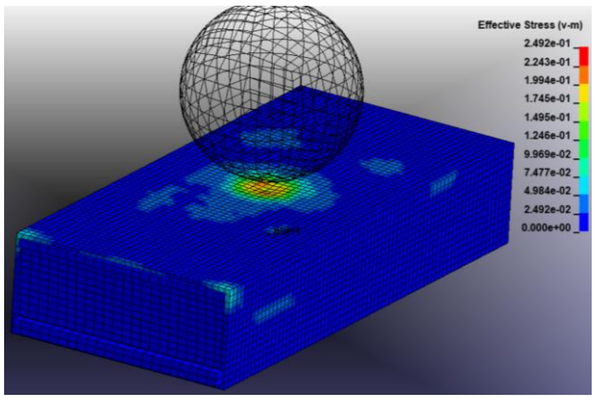

Figure 38 Battery impact zone: Time: 10 m/s Von Misses Maximum Stress = .2492 Pa

Time: 10 m/s Von Misses Maximum Stress= .2492 Pa

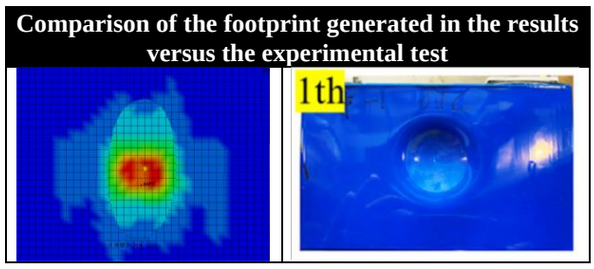

Table 1 Comparison of the generated footprint.

Acknowledgements

I thank the Doctors who supported me so that it was possible to finish writing this article. I thank my family for supporting me and allowing me to continue to achieve my goals, especially my parents because they gave me their support so that I could follow this path of knowledge.

Conclusions

The deformations resulting from the numerical simulation are congruent with those presented experimentally. Deformations that are at low speeds but that manage to deform the battery, which will affect the correct operation of a battery of these characteristics.

The lithium-ion battery studied in this work presents conditions of easy deformation. Therefore, the necessary precautions must be taken for its use under the load conditions presented.

References

Beauregard, Garret P., & Phoenix. (2008). *Informe de Investigación: Híbridos más vehículo hibrido eléctrico enchufable.*

Chen, X., Yuan, Q., Wang, T., Ji, H., Ji, Y., Li, L., & Liu, Y. (2020). Experimental study on the dynamic behavior of prismatic lithium-ion battery upon repeated impact. *Engineering Failure Analysis*, *115*, 104667. https://doi.org/10.1016/j.engfailanal.2020.104667

Departamento de Transporte de EE. UU. (2012). *Informa general de incidentes de batería de voltios de Chevrolet*.

Feng, X., Ouyang, M., Liu, X., Lu, L., Xia, Y., & He, X. (2018). Thermal runaway mechanism of lithium ion battery for electric vehicles: A review. *Energy Storage Materials*, *10*, 246–267. https://doi.org/10.1016/J.ENSM.2017.05.013

FERDINAND P. BEER. (2015). *MECÁNICA DE MATERIALES* (E. RUSSELL JOHNSTON, DEWOLF T., & MAZUREK F. DAVID, Eds.; SÉPTIMA EDICIÓN). Mc Graw Hill.

Greve, L., & Fehrenbach, C. (2012). Mechanical testing and macro-mechanical finite element simulation of the deformation, fracture, and short circuit initiation of cylindrical Lithium ion battery cells. *Journal of Power Sources*, *214*, 377–385. https://doi.org/10.1016/j.jpowsour.2012.04.055

Iglesias, R., Lago, A., Nogueiras, A., Martínez-Peñalver, C., Marcos, J., Quintans, C., & Moure, M. (2012). *Modelado y Simulación de una Batería de Ion-Litio Comercial Multicelda*.

JOHN O. HALLQUIST. (2006). *LS-DYNA THEORY MANUAL* (Livermore Software).

Los coches eléctricos están provocando nuevos protocolos de emergencia debido a las baterías y sus riesgos de incendio. (n.d.). Retrieved May 7, 2023, from https://www.xataka.com/vehiculos/coches-electricos-estan-provocando-nuevos-protocolos-emergencia-debido-baterias-sus-riesgos-incendio

Meng, L., See, K. W., Wang, G., Wang, Y., Zhang, Y., Zang, C., & Xie, B. (2022). Explosion-proof lithium-ion battery pack – In-depth investigation and experimental study on the design criteria. *Energy*, *249*, 123715. https://doi.org/10.1016/j.energy.2022.123715

NFPA. (n.d.). Retrieved May 7, 2023, from https://www.nfpa.org/

STEPHEN P. TIMOSHENKO. (1972). *MECHANICS OF MATERIALS* (GERE J. M., Ed.).

Wang, Q., Mao, B., Stoliarov, S. I., & Sun, J. (2019). A review of lithium ion battery failure mechanisms and fire prevention strategies. *Progress in Energy and Combustion Science*, *73*, 95–131. https://doi.org/10.1016/j.pecs.2019.03.002

Yu, D., Ren, D., Dai, K., Zhang, H., Zhang, J., Yang, B., Ma, S., Wang, X., & You, Z. (2021). Failure mechanism and predictive model of lithium-ion batteries under extremely high transient impact. *Journal of Energy Storage*, *43*, 103191. https://doi.org/10.1016/j.est.2021.103191

Zhang, X., Sahraei, E., & Wang, K. (2016). Deformation and failure characteristics of four types of lithium-ion battery separators. *Journal of Power Sources*, *327*, 693–701. https://doi.org/10.1016/j.jpowsour.2016.07.078

ISSN-On line: 2444-4987

Article **Journal of Research and Development**
June 2023, Vol.9 No.23 10-16

Use of a smartwatch for home blood pressure measurement

Uso de un reloj inteligente para la medición doméstica de la presión arterial

MEX-ÁLVAREZ, Rafael Manuel de Jesús†*, GUILLEN-MORALES, María Magali, YANEZ-NAVA, David and NOVELO-PÉREZ, María Isabel

Universidad Autónoma de Campeche, Facultad de Ciencias Químico-Biológicas, México.

ID 1st Author: *Rafael Manuel de Jesús, Mex-Álvarez*

ID 1st Co-author: *María Magali, Guillen-Morales*

ID 2nd Co-author: *David, Yanez-Nava*

ID 3rd Co-author: *María Isabel, Novelo-Pérez*

DOI: 10.35429/JRD.2023.23.9.10.16 Received: January 10, 2023; Accepted: June 30, 2023

Abstract

The use of smart watches represents an advantage in home monitoring of ambulatory patient blood pressure; but it is necessary to know the degree of correspondence with the conventional equipment for a better control of the blood pressure that is of clinical utility, in the present study the correlation of the values of the blood pressure obtained by a digital baumanometer and by a watch was evaluated. intelligent in young males at rest and after exercise; the results obtained show a good correlation between the measurements obtained by both teams (R2 values greater than 0.7), the cautious use of smart watches is useful for better monitoring of blood pressure and presents advantages such as automatic and digital recording of the values that can be used for ambulatory blood pressure monitoring.

Environmental monitoring, Baumanometer, Blood pressure

Resumen

El uso de relojes inteligentes representa una ventaja en el monitoreo doméstico de la presión arterial de pacientes ambulatorios; pero se precisa conocer el grado de correspondencia con los equipos convencionales para una mejor control de la presión arterial que sea de utilidad clínica, en el presente estudio se evalúo la correlación de los valores de la presión arterial obtenidos por un baumanómetro digital y por un reloj inteligente en varones jóvenes durante el reposo y posterior al ejercicio; los resultados obtenidos muestran una buena correlación entre las medidas obtenidas por ambos equipos (valores de R2 superior a 0.7), el uso cauteloso de relojes inteligentes es útil para un mejor monitoreo de la presión arterial y presenta ventajas como el registro automático y digital de los valores que pueden emplearse para un monitoreo ambulatorio de la presión arterial.

Monitoreo ambiental, Baumanómetro, Presión arterial

Citation: MEX-ÁLVAREZ, Rafael Manuel de Jesús, GUILLEN-MORALES, María Magali, YANEZ-NAVA, David and NOVELO-PÉREZ, María Isabel. Use of a smartwatch for home blood pressure measurement. Journal of Research and Development. 2023. 9-23:10-16.

* Author's Correspondence (E-mail: rafammex@uacam.mx)
† Researcher contributing as first author.

Article Journal of Research and Development
June 2023, Vol.9 No.23 10-16

Introduction

The reliable measurement of blood pressure is important because it allows the correct classification of a patient's risk; although this procedure may seem simple, it can lead to complications such as errors in the reading by the personnel performing the measurement, who must be trained and qualified in the use and handling of the device and use a reliable and valid apparatus. In this sense, the device considered the gold standard is the mercury sphygmomanometer; but these devices have the disadvantage that they are currently in disuse due to the risk to environmental health and are being replaced by digital devices such as digital manometers and smart watches1-4.

Therefore, it is inferred that the alternatives for measuring blood pressure must be calibrated periodically and comply with a minimum of pre-established clinical criteria to avoid erroneous or non-validated data; With the rise of smart watches that incorporate cardiovascular measurement systems such as pulsimeters, oximeters and baumanometers, they can be included as auxiliary tools in the monitoring of blood pressure in ambulatory patients to obtain blood pressure records throughout the day, as they are easily connected to mobile phones that record this data and present it in a simple graphic form2,3,5-7. The aim of the present study was to evaluate the correlation of existing blood pressure measurements between those obtained by a digital blood pressure monitor and a smart watch, in order to determine the usefulness of using these devices in a compensatory and practical way in patients of working age and with social commitments that would prevent them from adequately controlling their health and carrying out a more effective therapeutic follow-up.

Methodology

A descriptive cross-sectional study was conducted in which volunteer participants who filled out the informed consent form were registered and asked to complete a standardised and validated digital questionnaire (eHEALS) that measures a patient's basic digital health literacy8.

During the measurement, a trained research assistant performed the blood pressure measurements using the digital baumanometer and by placing the smartwatch with blood pressure monitor on the wrist and recorded the blood pressure readings. Blood pressure was taken from the left arm or wrist while the subject remained seated, without talking, without crossing the legs and resting the arm on a flat surface at the level of the heart; it was measured initially in a resting state9, after the initial interview we waited 10 minutes for the patient to relax, then asked the patient to walk up and down 60 steps of 15 cm each, and after 5 minutes blood pressure was measured again with both devices.

The demographic characteristics of the study cohort are: 26 young Latino males aged 20-23 years with no history of chronic diseases such as diabetes or hypertension, normal height, weight and body mass index (between 20 and 22), non-smokers and non-caffeine users; The blood pressure data were processed in Excel® and box and whisker plots were obtained for all values obtained and linear regression analysis was performed to measure the correspondence of the data from the digital baumanometer and the smart watch, from which the equation of the line and the correlation coefficient, R, were obtained.

Results and discussion

In this study it was decided to include only normotensive males to rule out any interference of the disease or antihypertensive pharmacotherapy in the results, although the aim of this work was to compare the measurements made by a smart watch with those obtained with a conventional digital blood pressure monitor commonly used in clinical practice, women were not included because the exact effect of the menstrual cycle on blood pressure during physical activity or exercise is not known9.

The blood pressure values obtained from the measurements of the young volunteers are reported in table 1 and figure 1, these values are consistent with those reported for healthy, non-hypertensive young people as optimal blood pressure is considered to be <120 mmHg for systolic and <80 mmHg for diastolic and normal <130 mmHg and <85 mmHg, respectively10,11.

ISSN-On line: 2444-4987

Although frequent exercise has a hypotensive effect in hypertensive patients due to different mechanisms such as decreased peripheral vascular resistance, decreased plasma renin activity, reduced body weight and body fat, among others, it tends to increase slightly immediately after physical activity and normalises and decreases from baseline; In this study we did not inquire about their physical activity habits that would influence post-exercise blood pressure, since an individual accustomed to practising some physical activity tends to lower their blood pressure due to better breathing control and a more adequate cardiovascular response9,12-15.

	PSB	PSR	PDB	PDR	PSB*	PSR*	PDB*	PDR*
MIN	107	109	67	69	109	113	70	73
Q1	113	116	70	73	117	119	75	77
Q2	116	118	73	75	118	122	76	79
Q3	119	120	77	77	122	124	78	81
MAX	127	126	86	82	129	132	81	85
X	116	118	74	75	119	122	76	79
DE	5	4	5	3	5	5	3	3

Table 1 Pressure values obtained in healthy male volunteers (n=26) measured at rest and after moderate exercise (the first 2 letters denote Systolic Pressure, SP, or Diastolic Pressure, DP, the last letter denotes the measuring device, B is bathometer and R is electronic clock, post-exercise status is denoted by *; Min group minimum value, Max group maximum value, X mean, SD standard deviation, Q quartile, X-quartile.)
Source: Own elaboration with the results of the research

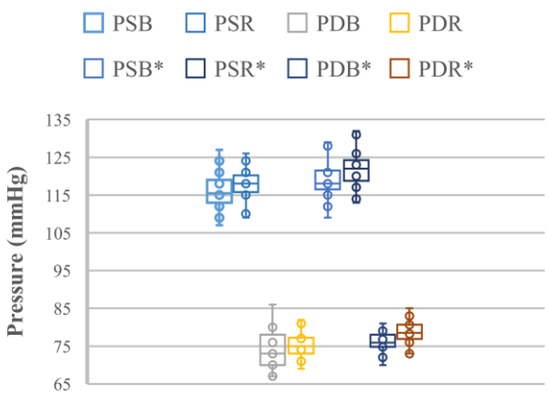

Graphic 1 Distribution of pressure values obtained in healthy male volunteers (n=26) measured at rest and after moderate exercise (the first 2 letters denote Systolic pressure, SP, or Diastolic pressure, DP, the last letter denotes the measuring device, B is bathometer and R is electronic clock, the post-exercise state is denoted by *, the last letter denotes the measuring device, B is bathometer and R is electronic clock, the post-exercise state is denoted by *)
Source: Own elaboration with the results of the research

The correspondence of the blood pressure measurements at rest (figure 2) was acceptable, a better correlation was obtained between the data obtained in both instruments in the systolic pressure (R2=0.7365) with respect to the correlation in the diastolic pressure (R2=0.707), as it was observed that the smart watch was more accurate at higher values of pressure; the same was observed in the values of blood pressure after exercise as the R2 values in this case were 0. 7818 for diastolic and 0.8852 for systolic, corroborating the assertion that the smartwatch is less sensitive than the blood pressure cuff and requires a higher pressure value to obtain a similar reading; this is of great clinical importance because accurate pressure measurement is a critically important characteristic as an error in pressure reading of more than five millimetres of mercury can lead to misclassification of the patient. In addition to the measuring equipment, one of the factors that most influences the recording of blood pressure is the analyst, which is why he or she must be trained initially and periodically. In this study, a single analyst participated who was trained to take all the measurements in order to rule out variation due to different analysts; it should be noted that the existence of technical errors in taking blood pressure is not mutually exclusive, but rather their effects are additive6,16.

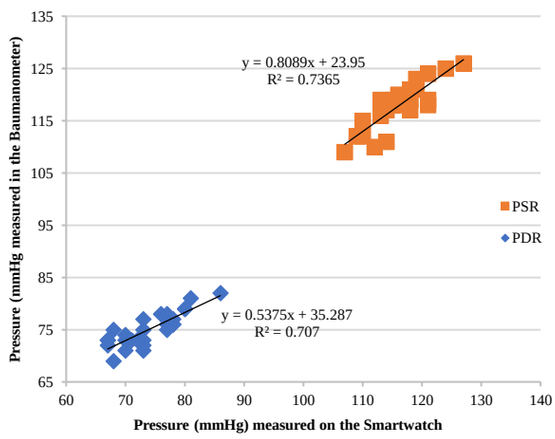

Graphic 2 Correlation of pressure values obtained in healthy male volunteers (n=26) measured during the resting state (PSR resting systolic pressure, PDR resting diastolic pressure, PDR resting diastolic pressure, PDR resting diastolic pressure, PDR resting systolic pressure, PDR resting diastolic pressure, PDR resting diastolic pressure, PDR resting diastolic pressure)
Source: Own elaboration with the results of the research

ISSN-On line: 2444-4987

The importance of knowing the correlation of blood pressure values obtained by two instruments, one frequently used and the other recently introduced, is to know the reliability of the measurements made by the latter and to be able to use it in environmental blood pressure monitoring (ABPM) because it has the advantage of being portable or wearable, which allows blood pressure to be recorded periodically during the daily routine; in addition to this, smart watches can be attached to mobile phones and the pressure is recorded in their own application for subsequent analysis3,7,17-19.

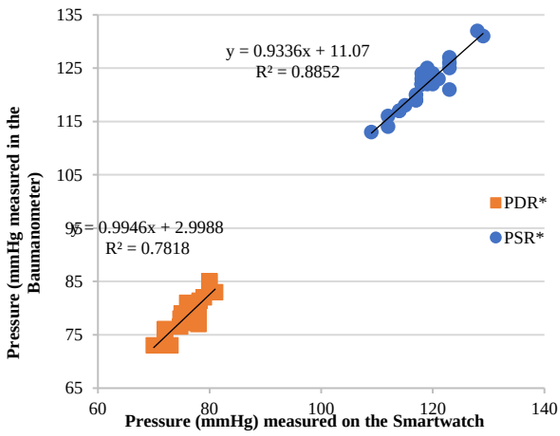

Graphic 3 Correlation of blood pressure values obtained in healthy male volunteers (n=26) measured during the post-exercise state (PSR* post-exercise systolic pressure, PDR* post-exercise diastolic pressure, PDR* post-exercise diastolic pressure, PSR* post-exercise systolic pressure, PDR* post-exercise diastolic pressure, PDR* post-exercise diastolic pressure)
Source: Own elaboration with the results of the research

Similarly, the values of the slope (m) and the intersection of the ordinate (b) in the equation of the line obtained in each case describe an increase in correspondence and sensitivity with increasing blood pressure; this is best seen in figure 4, where the pressure values at the two times, at rest and after exercise, are compared. This is consistent with the results found by Falter et al. (2022), in their study they found a systematic bias that overestimated low readings and underestimated high readings; they also stress the importance of creating standards for these reading devices for clinical use, a substantial difference with this study is that the volunteers participated in the measurement and were medicated hypertensives18.

In general, studies agree with this work on the accuracy of smartwatches in controlled conditions, as Kario et al. (2020) found that office-based measurement (as in this paper) was more accurate than ambulatory measurement; However, it should be used with caution and the device should be properly calibrated; this represents an opportunity for improvement to establish criteria for its use and to take advantage of the advantages it offers, especially in ABPM, such as its use in patients with chronic diseases, and to bear in mind that each smartwatch has its own characteristics of the manufacturer and will also depend on its generation, as this device (gadget) becomes more popular it will surely obtain improvements in its design that will allow it to increase its accuracy17-22.

In the same vein, although blood pressure monitoring using a calibrated smartwatch is feasible for domestic and ambulatory measurements, precautions should be taken regarding its use in the real world environment such as at home and in the office and technical specifications such as optimal recalibration time, training for proper use and data acquisition should be taken into account; it should also be noted that good support in pharmaceutical care would help to solve many of these problems and promote pressure control and therapeutic adherence 20-24.

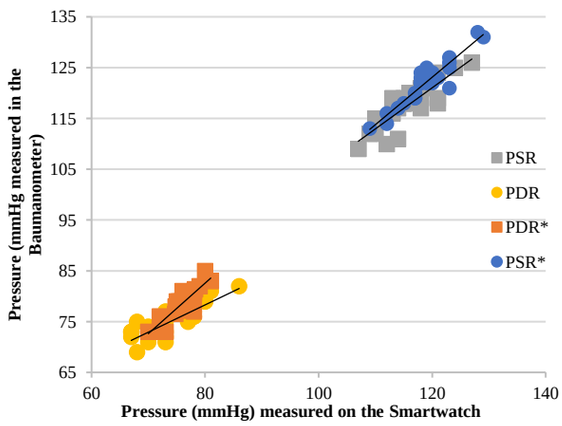

Graphic 4 Correspondence of pressure values obtained in healthy male volunteers (n=26) measured at rest and after moderate exercise (the first 2 letters denote systolic pressure, SP, or diastolic pressure, DP, the last letter denotes the measuring device, B is bathometer and R is electronic clock, the post-exercise state is denoted with *)
Source: Own elaboration with the results of the research

ISSN-On line: 2444-4987

Conclusions

The blood pressure values of young men, at rest and after exercise, measured with the smart watch correlate well with those obtained with the digital bathometer; it was observed that this correlation improves when a higher blood pressure value is recorded, suggesting a lower measurement sensitivity in the digital watch; the measuring instruments should be calibrated to adjust their values and allow a reliable measurement that allows adequate monitoring of the patient's pressure and provides useful data in clinical and pharmaceutical follow-up.

References

1. Fuentes, R., & Bañuelos, M. A.. (2004). Digital blood pressure monitor. *Journal of applied research and technology*, 2(3), 224-229.

2. González-Rivas, J. P. (2016). Optimizando la medición de la presión arterial en la consulta. *Revista Venezolana de Endocrinología y Metabolismo*, *14*(3), 179-186.

3. Galván-Oseguera, H., Rosas-Peralta, M., Borrayo-Sánchez, G., González-Díaz, B.E., Almeida-Gutiérrez, E., Ramírez-Arias, E., & Pérez-Rodríguez, G. (2019). Formas de medición de la presión arterial sistémica: el debate continúa. *Medicina interna de México*, *35*(1), 104-112. https://doi.org/10.24245/mim.v35i1.2458

4. Bhanvadia, S.B., Manreet S.B., Arash Delavar, K.T., Bharanidharan, R., Saseendrakumar, R.N., Weinreb, L.M.Z., & Sally, L.B. (2022). Assessing Usability of Smartwatch Digital Health Devices for Home Blood Pressure Monitoring among Glaucoma Patients" *Informatics*, *9*(4), 79. https://doi.org/10.3390/informatics9040079

5. Cardona-Müller, D., Grover-Páez, F., Guzmán-Saldivar, V., Alanis-Sánchez, G.A., Murguía-Soto, C., Totsuka-Sutto, S.E., Quezada-Fernández, P., Macías-Chumacera, A., Cardona-Muñoz, E.G., & Ramos-Becerra, C.G. (2018). Confiabilidad de un monitor automatizado para la medición de la presión arterial. *Revista médica de Chile*, *146*(2), 190-195. https://dx.doi.org/10.4067/s0034-98872018000200190

6. Padwall, R., Campbell, N.R.C., Schutte, A.E., Olsen, M.H., Delles ,C., Etyang, A., Cruickshank, J.K., Stergiou, G., Rakotz, M.K., Wozniak, G., Jaffe, M.G., Benjamin, I., Parñati, G., Sharman, J.E. (2020). Optimización del desempeño del observador al medir la presión arterial en el consultorio: declaración de posición de la Comisión Lancet de Hipertensión. *Rev Panam Salud Publica*, *44*, e88. https://doi.org/10.26633/RPSP.2020.88

7. Yen, H. Y., & Huang, W. H. (2022). The efficacy of commercial smartwatches with a blood pressure-monitoring feature: A pilot randomized controlled trial. *Journal of nursing scholarship : an official publication of Sigma Theta Tau International Honor Society of Nursing*, *54*(3), 324–331. https://doi.org/10.1111/jnu.12740

8. Paramio Pérez, G., Almagro, B.J., Hernando Gómez, A., & Aguaded Gómez, J.I. (2015). Validación de la escala eHealth Literacy (eHEALS) en población universitaria española. *Revista Española de Salud Pública*, *89*(3), 329-338. https://dx.doi.org/10.4321/S1135-57272015000300010

9. Gamboa Granados, M., & Solera Herrera, A. (2014). Efecto agudo de dos intensidades de ejercicio aeróbico sobre la presión arterial en reposo de personas normotensas. *Revista Andaluza de Medicina del Deporte*, *7*(3), 101-105.

10. Valero, R., & García Soriano, A. (2009). Normas, consejos y clasificaciones sobre hipertensión arterial. *Enfermería Global*, (15).

ISSN-On line: 2444-4987

11. Sánchez, R.A., Ayala, M., Baglivo, H., Velázquez, C., Burlando, G., Kohlmann, O., Jiménez, J., López Jaramillo, P., Brandao, A., Valdés, G., Alcocer, L., Bendersky, M., Ramírez, A.J., & Zanchetti, A. (2010). Guías Latinoamericanas de Hipertensión Arterial. *Revista chilena de cardiología*, *29*(1), 117-144. https://dx.doi.org/10.4067/S0718-85602010000100012

12. Álvarez-Aguilar, P. (2015). Efectos agudos del ejercicio en la presión arterial. Implicaciones terapéuticas en pacientes hipertensos. *Acta Médica Costarricense*, *57*(4), 163-171.

13. Cordente Martínez, C.A., García Soidán, P., Sillero Quintana, M., & Domínguez Romero, J. (2007). Relación del nivel de actividad física, presión arterial y adiposidad corporal en adolescentes madrileños. *Revista Española de Salud Pública*, *81*(3), 307-317.

14. Álvarez, C., Olivo, J., Robinson, O., Quintero, J., Carrasco, V., Ramírez-Campillo, R., Andrade, D.C., & Martínez, C. (2013). Efectos de una sesión de ejercicio aeróbico en la presión arterial de niños, adolescentes y adultos sanos. *Revista médica de Chile*, *141*(11), 1363-1370. https://dx.doi.org/10.4067/S0034-98872013001100001

15. Bermúdez, C. (2012). Valoración de la presión arterial en la ergometría. *Revista Uruguaya de Cardiología*, *27*(3), 399-404.

16. Vázquez, J.A., Savelli, C., Terán, R., Tirado, S.S., Uzcátegui, Y.B., Vargas, R.E., & Zamora, F.A. (2001). Técnica de Medición de la Presión Arterial Utilizada por Enfermeras Auxiliares del Hospital Universitario de Caracas. *Revista de la Facultad de Medicina*, *24*(1), 80-87.

17. Sandoya, E. (2013). Estado actual del monitoreo ambulatorio de presión arterial. *Revista Uruguaya de Cardiología*, *28*(2), 273-284

18. Falter, M., Scherrenberg, M., Driesen, K., Pieters, Z., Kaihara, T., Xu, L., Caiani, E. G., Castiglioni, P., Faini, A., Parati, G., & Dendale, P. (2022). Smartwatch-Based Blood Pressure Measurement Demonstrates Insufficient Accuracy. *Frontiers in cardiovascular medicine*, *9*, 958212. https://doi.org/10.3389/fcvm.2022.958212

19. van Helmond, N., Freeman, C. G., Hahnen, C., Haldar, N., Hamati, J. N., Bard, D. M., Murali, V., Merli, G. J., & Joseph, J. I. (2019). The accuracy of blood pressure measurement by a smartwatch and a portable health device. *Hospital practice (1995)*, *47*(4), 211–215. https://doi.org/10.1080/21548331.2019.1656991

20. Kario, K., Shimbo, D., Tomitani, N., Kanegae, H., Schwartz, J. E., & Williams, B. (2020). The first study comparing a wearable watch-type blood pressure monitor with a conventional ambulatory blood pressure monitor on in-office and out-of-office settings. *Journal of clinical hypertension (Greenwich, Conn.)*, *22*(2), 135–141. https://doi.org/10.1111/jch.13799

21. Ahn, J. H., Song, J., Choi, I., Youn, J., & Cho, J. W. (2021). Validation of Blood Pressure Measurement Using a Smartwatch in Patients With Parkinson's Disease. *Frontiers in neurology*, *12*, 650929. https://doi.org/10.3389/fneur.2021.650929

22. Han, M., Lee, Y. R., Park, T., Ihm, S. H., Pyun, W. B., Burkard, T., Cho, M. C., Camafort, M., Yang, E., Stergiou, G. S., Lee, H. Y., Seo, J. M., & Korean Society of Hypertension (2023). Feasibility and measurement stability of smartwatch-based cuffless blood pressure monitoring: A real-world prospective observational study. *Hypertension research : official journal of the Japanese Society of Hypertension*, *46*(4), 922–931. https://doi.org/10.1038/s41440-023-01215-z

ISSN-On line: 2444-4987

23. García-Falcón, D., Lores-Delgado, D., Dupotey-Varela, N.M, & Espino-Leyva, D.L. (2018). Atención Farmacéutica en adultos mayores hipertensos. Una experiencia en la atención primaria de salud en Cuba. *Ars Pharmaceutica (Internet)*, *59*(2), 91-98. https://dx.doi.org/10.30827/ars.v59i2.7307

24. Ortega, C.B., Rodríguez, G., Aguilar-Rabito, A., Samaniego, L., & Larroza, G.M. (2022). Adherencia a la medicación mediante el uso del teléfono en pacientes hipertensos crónicos. *Revista CON-CIENCIA*, *10*(1), 17-32. https://doi.org/10.53287/tmph6198gn62f

Article **Journal of Research and Development**
June 2023, Vol.9 No.23 17-28

Strain localization instability in seafloor spreading centers of the Carmen Basin, southern Gulf of California

Inestabilidad de la localización de la deformación en los centros de extensión del fondo marino de la Cuenca del Carmen, sur del Golfo de California

JULIÁ-MIRALLES, Marc†, YARBUH, Ismael*, SPELZ, Ronald M. and NEGRETE-ARANDA, Raquel

Universidad Autónoma de Baja California, Facultad de Ciencias Marinas, Departamento de Geología, Campus Ensenada, Baja California, México.

ID 1st Author: *Marc, Juliá-Miralles* / **ORC ID:** 0000-0001-8201-3566, **CVU CONAHCYT ID:** 1011828

ID 1st Co-author: *Ismael, Yarbuh* / **ORC ID:** 0000-0002-7146-3841, **CVU CONAHCYT ID:** 381344

ID 2nd Co-author: *Ronald M., Splez* / **ORC ID:** 0000-0002-9561-355X, **CVU CONAHCYT ID:** 37229

ID 3rd Co-author: *Rauqel, Negrete-Aranda* / **ORC ID:** 0000-0003-3049-4374, **CVU CONAHCYT ID:** No. 92968

DOI: 10.35429/JRD.2023.23.9.17.28 Received: January 20, 2023; Accepted: June 30, 2023

Abstract

This study provides new insights into the geological evolution of the Carmen Basin (CB) in the southern Gulf of California (GC). Using high-resolution bathymetry and seismic reflection profiles, we establish a plate-kinematic framework for this oblique-divergent rift system. By analyzing the crustal composition, we investigate the growth of the bounding transform faults and their role in accommodating transtensional shearing. We propose that the mantle upwelling beneath the CB is a northward extension of the East Pacific Rise. The CB consists of three sub-basins with distinct geometries, morphologies, and evolutionary histories. While the southern and central sub-basins are mostly abandoned, the northern sub-basin is currently experiencing seafloor spreading. This is supported by the presence of younger oceanic crust, approximately less than 1.5 Ma, juxtaposed with older oceanic crust that aligns in age with the nearby Guaymas and Farallon basins to the north and south, respectively. Our findings also indicate favorable geological conditions in the CB for the development of hydrothermal systems similar to those observed in the neighboring Guaymas and Pescadero basins in the southern GC.

Simple shear deformation, Crustal lithology, Fast seafloor spreading

Resumen

El presente trabajo proporciona nuevos conocimientos sobre la evolución geológica de la Cuenca de Carmen (CB) en el sur del Golfo de California (GC). A partir de datos de batimetría de alta resolución y perfiles sísmicos de reflexión, establecemos la cinemática de la tectónica de placas para este sistema de rift oblicuo-divergente. Al analizar la composición de la corteza, investigamos el crecimiento de las fallas transformes y el papel que juegan estas para acomodar la cizalla transtensional. Proponemos que el ascenso del manto por debajo de la CB es una extensión de la dorsal del Pacífico Oriental. La CB consta de tres sub-cuencas con geometrías, morfologías e historias evolutivas distintas. Mientras que las sub-cuencas del sur y del centro están prácticamente abandonadas, la sub-cuenca del norte está experimentando actualmente la expansión activa del fondo marino. Esto se apoya en la presencia de corteza oceánica más joven, aproximadamente menor que 1.5 Ma, asociada con una corteza oceánica más antigua que tiene la misma edad que las cuencas de Guaymas y Farallón que delimitan a la CB hacia el norte y sur, respectivamente. Nuestros resultados también indican condiciones geológicas favorables en la región para el desarrollo de sistemas hidrotermales similares a los observados en las cuencas vecinas de Guaymas y Pescadero en el sur del GC.

Deformación por cizalla simple, Litología de la corteza, Rápida dispersión del fondo marino

Citation: JULIÁ-MIRALLES, Marc, YARBUH, Ismael, SPELZ, Ronald M. and NEGRETE-ARANDA, Raquel. Strain localization instability in seafloor spreading centers of the Carmen Basin, southern Gulf of California. Journal of Research and Development. 2023. 9-23:17-28.

* Author's Correspondence (E-mail: uyarbuh@uabc.edu.mx)
† Researcher contributing as first author.

Introduction

The rifting dynamics of the Gulf of California (GC) still remain considerable gaps in information due to unexplored regions in the southern GC (Figure 1), where geological data has poor spatial and temporal resolution (Sutherland et al., 2012; Martín-Barajas et al., 2013; Macias-Iñiguez et al., 2019; Ramírez-Zerpa et al., 2022). The southwestern margin of the GC experiences active rifting, accompanied by east-directed low-angle normal faults and simple shear zones (Buck, 1988; Wernicke and Axen, 1988; Lavier et al., 1999; Fletcher and Spelz, 2009; Umhoefer et al., 2020; Figure 1). These structures accommodate significant crustal extension along the San Juan de Los Cabos and San Juan de Los Planes faults (Fletcher et al., 2000; Fletcher and Munguia, 2000; Bot et al., 2016), resulting in ~40 km of linear extension towards the continental-oceanic crust transition east of the Cerralvo basin, adjacent to the deep-water Pescadero basin complex (Figure 1; Macias-Iñiguez et al., 2019; Ramírez-Zerpa et al., 2022).

This study focuses on providing new insights into the structural evolution of the Carmen Basin (CB) from high-resolution bathymetry (Figure 2) and two-dimensional (2D) seismic reflection profiles (Figure 3-5). We characterize the geometry and structure of the CB to identify crustal deformation, basement lithology, seismic-stratigraphy, and magmatic events. Finally, we contrast our results with mantle tomography data (Wang et al., 2009; Di Luccio et al., 2014; Ferrari et al., 2018) to reconstruct the structural evolution of the CB, and discuss how the opening of the GC contributes to the formation of new oceanic crust, the deformation of the oceanic lithosphere to accommodate younger spreading centers, and the kinematics of the transform faults that constitute the modern Pacific and North America plate boundary.

Tectonic evolution of the Gulf of California

The northwestern continental margin of Mexico has undergone a significant transformation from a convergent plate boundary to an oblique-divergent margin (Balestrieri et al., 2017). During the Paleogene, the Farallon oceanic plate subducted beneath North America, creating a divergent plate boundary between the Farallon plate and the Pacific plate.

During the Eocene, the Farallon plate was largely consumed, and a portion of the East Pacific Rise approached the paleo-trench (Atwater, 1970; Stock and Hodges, 1989; Bunge and Grand, 2000; Wright et al., 2016). In the Oligocene, direct interaction occurred between the East Pacific Rise and the paleo-trench, and along the North American plate. The proximity of the Pacific-Farallon divergent margin to the continental borderland marked the transition from subduction to lithospheric extension and dextral shearing along the Magdalena plate boundary derived from the Farallon plate. Intraplate magmatism also occurred along the Baja Peninsula due to viscous shearing (Figure 1; Spencer and Normark, 1979; Atwater and Stock, 1998; Fletcher et al., 2007; Negrete-Aranda et al., 2013).

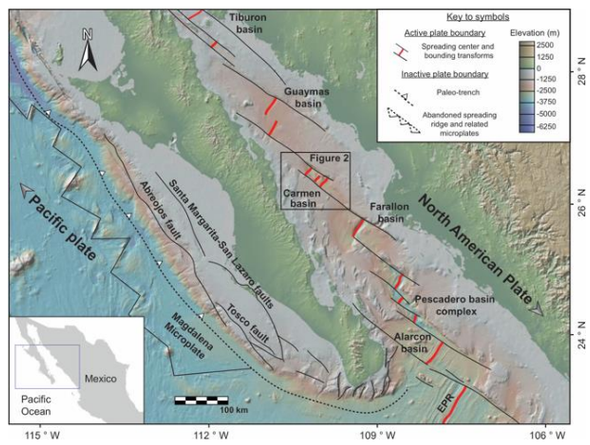

Figure 1 An overview of the tectonic features in the southern Gulf of California. It displays the plate motion (black arrows), the transform fault system (black lines), pull-apart basins, and spreading centers (red lines). The study area with the location of the Carmen Basin is denoted by the black box (Figure 2). Figure adapted from Julià-Miralles et al. (submitted). The abbreviation "EPR" is used for the East Pacific Rise. Base map sourced from GeoMapApp (http://www.geomapapp.org).

During the early Miocene, the Farallon plate fragmented into several smaller plates, with buoyant remnants of the Farallon plate and a section of the North American plate coupling with the Pacific Plate and moving northwestward (Nicholson et al., 1994; Bohannon and Parson, 1995). Dextral-oblique shearing migrated eastward from the continental margin into the current GC, leading to overall crustal thinning in the region (Stock and Hodges, 1989; Fletcher et al., 2007; Umhoefer et al., 2020).

ISSN-On line: 2444-4987

This process was accompanied by an increase in rift obliquity, facilitated by a change in plate motion direction, resulting in the localization of the plate boundary, marine incursion in the northern GC at ~8 Ma, and the formation of shallow water basins (Bennett et al., 2016; Umhoefer et al., 2018; Ramírez-Zerpa et al., 2022). The current tectonic regime was established ~6 Ma, when the East Pacific Rise extended into the mouth of the GC, separating the Baja California Peninsula from the North American continent (Wang et al., 2009, 2013; Lizarralde et al., 2007; Piñero-Lajas, 2008; Ramírez-Zerpa et al., 2022). Magma accretion was made possible by the propagation of right-lateral, right-stepping transform faults, which transferred motion oblique to the primary movement of the Baja California Microplate (Fletcher et al., 2007).

Methods

High-resolution bathymetry data was acquired for the CB basin during the FK210922 expedition in October 2021, conducted aboard the R/V Falkor and operated by the Schmidt Ocean Institute. The data was collected using an EM 302 multi-beam echo sounder, capturing 432 soundings per swath with dual swath mode for up to 864 soundings. The bathymetry data covered a depth of ~3,600 m and were gridded at 40-m intervals. The survey lines were spaced 5 km apart, running sub-parallel to the master transform faults that bound the basin.

Two dimensional (2D) seismic reflection data was used along ~65 km to constrain the rift evolution of CB. Data collected in 2006 aboard the R/V Francisco de Ulloa during a collaborative data collection campaign involving CICESE and Scripps Institution of Oceanography at UCSD. A three-stage workflow was applied to analyze the seismic data and generate sub-surface structural images. This workflow enabled frequency extraction, multiple mitigation, signal amplitude equalization, noise reduction, precise ray trajectory correction, spurious effect attenuation, and conversion from two-way travel time to depth (TWTT) to depth in meters (Yilmaz, 2001). Key structural features such as fault planes, folds, grabens, and sedimentary sequences were identified using well-proven criteria.

Quantitative parameters, such as fault length and dip, stratal thicknesses, subsidence, and sedimentary sequence boundaries, were also determined. Seismic facies analysis identified basement lithology and sedimentary material, including magmatic injections and geothermal fluids, in the form of mosaic patterns of highly reflective and low-reflectance surfaces (Chopra and Marfurt, 2007).

Results

Map view geometry of the Carmen Basin

The CB is a narrow, rhomboidal basin that has evolved from incipient to extremely mature basins. It is 80 km long and 20 km wide, with a length-to-width ratio of 4:1. Two sub-parallel, northwest-oriented principal displacement zones control the northeastern and southwestern margins of the CB. The Carmen transform fault extends 150 km, while the Farallon transform in the southwest stretches 200 km. These bounding zones overlap and connect through a traverse system of en-echelon oblique-extensional normal faults, creating three distinct sub-basins (Figure 2). The bathymetry of the CB reveals significant footwall uplift along the trace of the transform faults, which is accommodated by an array of en-echelon segmented basin sidewall faults developed on both flanks of the CB (Figure 2). Along these steep faults, gravitational instabilities develop, leading to rapid and episodic slumping and grain flows, forming distinct cliffs with landslide crowns and scarps along the basin's outer margin. However, the primary sediment routing system for infilling the CB appears to be a submarine dendritic drainage system originating from the tips of the principal displacement zones (Figure 2).

ISSN-On line: 2444-4987

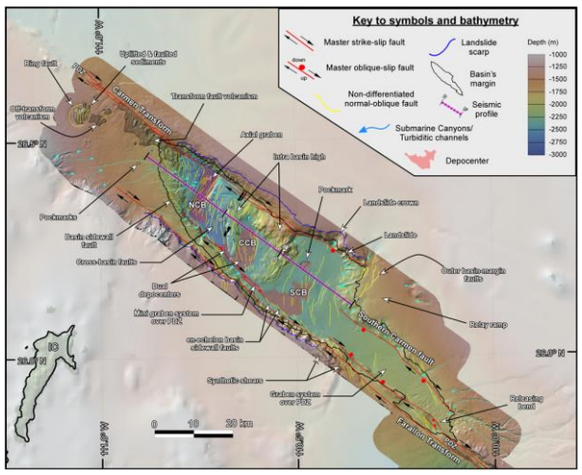

Figure 2 Structural map of the Carmen Basin (CB) illustrating its two-dimensional architecture and geometry. High-resolution (40-m) bathymetry is superimposed on faded GMRT bathymetry. Abbreviations: SCB = Southern Carmen Basin; CCB = Central Carmen Basin; NCB = Northern Carmen Basin. Figure adapted from Julià-Miralles et al. (submitted)

At a finer scale, Figure 2 reveals a cross-basin fault system that propagates obliquely to the principal displacement zones. This fault system originates a left-stepping arrangement of synthetic Riedel shear faults that curve into an elongated sigmoidal shape, connecting the sidewall faults at both sides of the basin. The resulting horst-graben structure divides the CB into three distinct sub-basins with contrasting morphologies, namely, the southern CB, the central CB, and the northern CB.

The southern CB features the shallowest depocenter (~2200 mbsl) among all the sub-basins, delimited by an array of cross-basin faults oriented at a high angle to the bounding transform faults (Figure 2). The northern margin is bounded by an uplifted and translated crustal block, while the southern margin is delimited by a strike-slip relay ramp that transfers and accommodates the deformation between the Carmen transform fault and a secondary oblique-slip fault called the "Southern Carmen fault." The relay ramp lies on the footwall of the oblique Southern Carmen fault, controlling a prominent graben system in the southeastern corner of the CB (Figure 2).

The central CB (~2400 mbsl) acts as a connection between the northern and southern CB. It is bordered by two intra-basin highs that have formed in response to a series of cross-basin faults that originate from synthetic Riedel shears along the basin's sidewalls (Figure 2).

These structural highs can be attributed to block translation and rotation during the early stages of basin development. The geometry of the central CB is elongated and oval, with a northern orientation, suggesting that deformation may have ceased in this region, allowing the modern northern CB spreading center to migrate further north (Figure 2). Variations in basin topography suggest the juxtaposition of different materials, with structural highs representing either a crystalline basement or indicating late Miocene-Pleistocene volcanic activity.

The northern CB represents the deepest part of the entire CB, reaching depths of ~2800 mbsl. The basin exhibits a broad nested graben where rocks have undergone downward displacement along an array of cross-basin faults connecting the bounding master faults (Figure 2). The overall geometry and geomorphological features of the northern CB suggest that the basin has evolved due to transtensional deformation, similar to the Pescadero basin complex located further south. The northern CB hosts the current seafloor spreading center, featuring a short and narrow axial graben oriented sub-perpendicular to the principal displacement zones (Figure 2). Magmatic activity is conspicuous not only across the spreading center but also along the bounding master faults and inside the sub-basins.

Crustal structure and stratigraphy of the Carmen Basin

The seismic interpretation of lines AA'-CC' (Figures 3-5) and morphology analysis reveal the structural evolution of the CB. The sub-basins exhibit two distinct seismic facies: high-energy successions and low-energy sequences. The first facies consists of rocks with prominent high-amplitude continuous reflectors, showing strong lateral coherence. This unit is likely composed of well-bedded pelagic sediments deposited in a low to medium-energy environment. The second facies consists of sedimentary rocks interbedded with and bounded by the distinct reflection of the first unit. Within the second rock unit, a diffuse seismic facies is observed, characterized by numerous short wavy reflections with poor lateral continuity, extending up to 1 km individually.

ISSN-On line: 2444-4987

These low-amplitude chaotic reflections represent higher energy accumulations of clastic sediments within the second seismic facies. The second facies appears dimmer than the first facies, giving the basin fill the appearance of thick accumulations of oceanic turbidites.

The seismic section also reveals a third facies characterized by a thick and homogeneous series of highly reflective, ropey-like layers with sigmoidal, semi-continuous reflection geometry and strong lateral coherence (Figures 3-5). These rocks exhibit more nonplanar reflections and limited lateral coherence, with individual reflections extending up to 1 km. The third unit spans a depth range from 2900 m at the depocenter of the actual axial graben to 1700 m in shallower sections (Julià-Miralles et al., submitted).

Profile AA' extends 28 km and images the southern CB, which trends NW-SE parallel to the axis of the CB (Figure 3). The profile shows a symmetrical horst-graben system delimited by two high-angle cross-basin faults, resulting in a topographic step of ~300 m in relief. The basin-bounding faults created sufficient subsidence to accommodate the deposition of ~550 m of syn-tectonic sedimentary sequences sourced from the continental shelf of the Baja California Peninsula and Sonora rifted margins. The most basal successions (~250 m-thick) have low-amplitude chaotic reflections, suggesting poor stratification and high-energy sedimentation (Figure 3). Growth strata sedimentation changes up-section to a seismic facies ~300 m-thick with good coherence and high-amplitude continuous reflections, suggesting low-medium energy sedimentation. The two seismic facies lie unconformably on the acoustic basement, interpreted as sigmoidal semi-continuous seismic reflections at 2800 m-depth on the southeastern flank of the symmetric graben and laterally terminate against the walls of an inactive nested fault system verging NW (Figure 3). The northwestern footwall block of the southern CB is interpreted to be a highly fractured oceanic basement, while the southeastern footwall block is covered by 300 m of sediments. The transition from horizontal sedimentation to a tilted configuration along a growing fault is interpreted to be the product of fault rotation, resembling negative flower structures Dooley and McClay, 1997; Wu et al., 2009; Julià-Miralles et al., submitted).

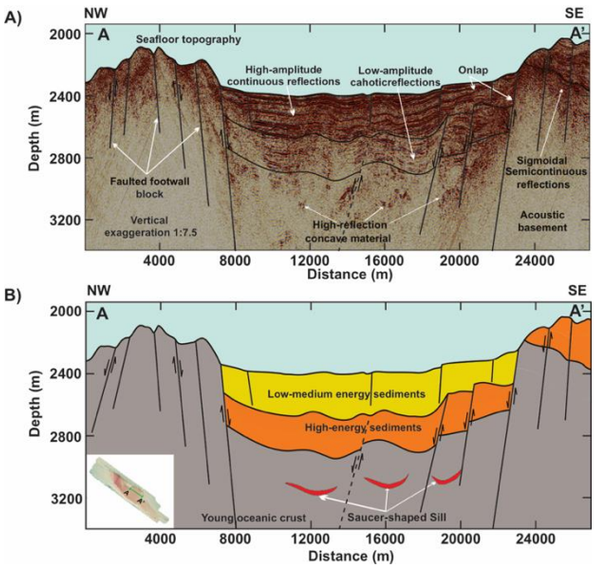

Figure 3 Seismic profile A-A' across the southern Carmen Basin (CB). A) Structural and stratigraphic seismic interpretation. B) Interpreted geologic cross-section. The seismic image reveals a wide, symmetrical graben bounded by two primary normal faults, identified as cross-basin structures (Figure 2). Panel (B) highlights high-amplitude reflections at ~3100 m depth, possibly indicating an ancient spreading center near abandoned nested normal faults. Figure adapted from Julià-Miralles et al. (submitted)

Profile BB' spans 20 km across the central CB (Figure 4), with high-amplitude curvy reflections indicating young oceanic crust. The central CB has an asymmetrical half-graben architecture, with a domino fault system defining the southern flank. The basal sedimentary package shows a pronounced tilt towards the SE, and the acoustic basement displays high-amplitude sigmoidal semi-continuous reflections at depths of 2800 m and 2400 m, suggesting an oceanic crust composed of volcanic flows. This material can be correlated with basement rocks in the southern CB, located further south of the CB. In the middle of the central CB (Figure 4), at a depth of 2700 mbsl, there is a 1 km-wide block of highly reflective material that stands above the well-defined basement to the NW. The seismic expression of this feature resembles the ropey textured reflections seen in the surrounding basement but appears brighter. It may indicate the axis of an extinct seafloor spreading system that was active prior to the deposition of the overlying sedimentary sequence (Figure 4). Above this feature and the surrounding oceanic basement, there is a syn-tectonic sedimentary package that reaches a thickness of ~300 m, showing seismic stratigraphy similar to the southern CB (Julià-Miralles et al., submitted).

ISSN-On line: 2444-4987

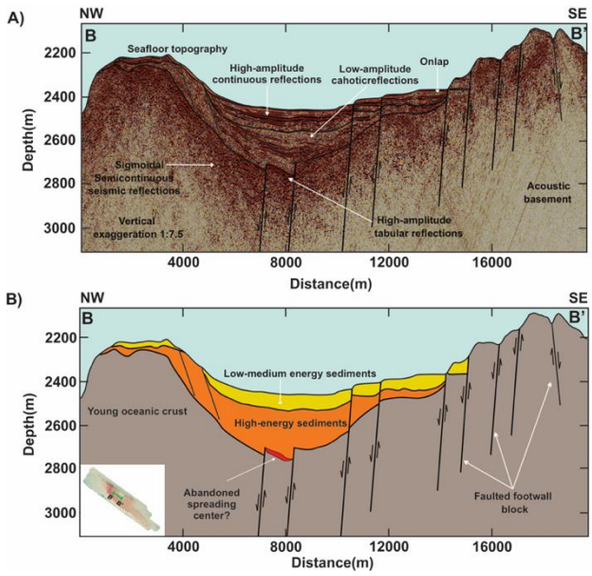

Figure 4 Seismic profile B-B' across the central Carmen Basin (CB). A) Structural and stratigraphic seismic interpretation. B) Interpreted geologic cross-section. The image reveals an asymmetrical half-graben structure NW-striking normal faults accommodating ~300 m of syn-tectonic sedimentation. In panel (B), at ~2750 m depth, tabular high-amplitude reflections suggest the presence of an ancient spreading center, similar to Figure 3. Figure adapted from Julià-Miralles et al. (submitted).

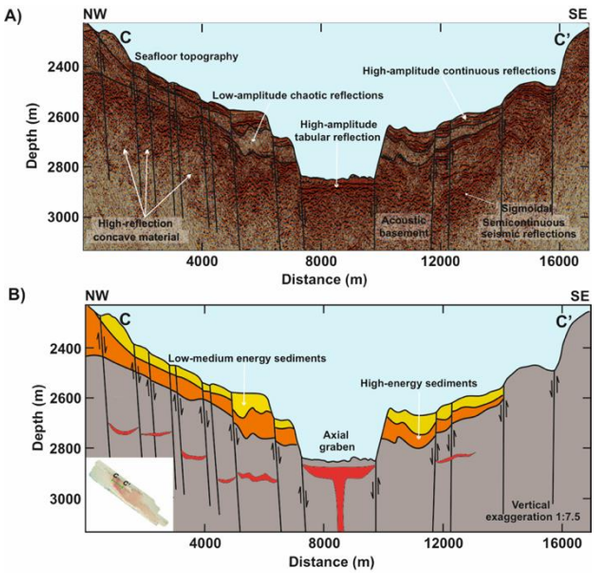

Figure 5 Seismic profile C-C' across the northern Carmen Basin (CB). A) Structural and stratigraphic seismic interpretation. B) Interpreted geologic cross-section. The profile intersects the axial graben of the northern CB. The spreading center is interpreted as asthenospheric mantle reaching the seafloor to generate new ocean crust. Figure adapted from Julià-Miralles et al. (submitted).

Profile CC' cuts through the northern CB with a length of 17 km, representing the deepest and narrowest sub-basin within the CB (Figure 5). The axial graben is bounded by inward-stepping normal faults striking perpendicular to the principal displacement zone. The sedimentary fill in the northern CB is notably thinner compared to other Carmen sub-basins, measuring only 200-300 m thick. The faults that define the margins of the innermost graben exhibit a throw of only 100 m, as indicated by the small steps observed on the top of the oceanic basement (Figure 5). The two seismic facies, characterized by high and low-amplitude reflection, are correlated on both flanks of the basin and are clearly dissected by the graben. On the southeastern flank of the axial graben, the sigmoidal semi-continuous reflections reach the seafloor topography at a depth of 2500 m, suggesting the young oceanic crust outcrops. On the northwestern flank of the axial graben, the oceanic basement is covered by the two sedimentary units interpreted throughout the CB. The inner graben represents the active spreading axis of the CB (Julià-Miralles et al., submitted; Figure 5).

Discussion

Crustal lithology and sill intrusion in the Carmen Basin

The CB acoustic basement is composed of highly reflective ropey layers with good lateral continuity, similar to those found in neighboring basins. These layers are identified as basaltic lava flows and intruded sills within sedimentary deposits (Piñero-Lajas, 2008; Lizarralde et al., 2007; Kluesner, 2011). The basement rocks outcrop widely along the three sub-basins of the CB, the spreading center, and the structural highs, forming approximately 80 km of newly formed oceanic crust. The Guaymas, Carmen, and Farallon basins are embedded in a slab of oceanic crust, with the eastern transition between continental and oceanic crust delimited by en-echelon scarps and the western and southwestern basin margins defined by rotated blocks along the Baja California continental shelf border (Macias-Iniguez et al., 2019). The CB separates the Guaymas and Farallon basins through an oceanic-oceanic crustal boundary, with the Carmen transform fault and Farallon transform fault bounding the CB being younger than the oceanic crust along the inner margins of the Guaymas and Farallon basins.

ISSN-On line: 2444-4987

The seismic profiles across the CB reveal concave, high-reflection material interpreted as saucer-shaped igneous sills, which are associated with overburden deformations, fluid migration through faults, and potential feeder networks (Negrete-Aranda, 2019, 2021; Sarkar et al., 2022; Julià-Miralles et al., submitted). These shallow sills are observed within a young oceanic crust, representing sites of magmatic crustal accretion in the actively growing basin. Off-axis intrusions into high-energy sediments are also identified between old oceanic crust and low-medium energy sediments.

Transform faults kinematics and crustal deformation in the Carmen basin

Mantle dynamics play a crucial role in the spreading rate of rift zones and core-complex accretion in mid-ocean ridge environments (Buck, 1993; Howell et al., 2019). Slow-spreading ridges exhibit buoyant mantle upwelling and focused melt migration beneath ridge centers, while fast-spreading ridges show uniform mantle upwelling along the ridge axis (Kuo and Forsyth, 1988; Lin et al., 1990; Escartin and Lin, 1995; Canales et al., 2000, 2003; Gregg et al., 2006, 2007). The formation of the CB in the southern GC is suggested to have occurred after seafloor spreading initiated in the Farallon and Guaymas basins. Kinematic instability of the bounding faults led to the propagation of the Carmen transform fault and Farallon transform fault, eventually forming the CB. The stability of this family of boundaries is influenced by the pooling of erupted lavas observed in topographic lows within the transform fault domain. This leaky magmatic accretion results from the presence of intermediate-fast-slipping transform faults, a configuration frequently observed at the East Pacific Rise (Gregg et al., 2007). The CB could be a result of an intra-transform spreading center system driven by fast rifting (Gregg et al., 2007; Gerya 2010; Julià-Miralles et al., submitted), where penetrative deformation along the main axis of the basin leads to different stages of deformation, resulting in the formation of sub-basins with contrasting geometries.

In the case of the CB, mantle upwelling and fast rifting were responsible for the formation of new oceanic spreading centers connected by intermediate-fast slipping transform faults (Wang et al., 2009; Zhao, 2004; Di Lluccio, 2014; Negrete-Aranda et al., 2021). The rapid formation of the CB (Umhoefer, 2011) may resolve the sequential abandonment of its sub-basins, with deformation progressing from the southeastern region of the CB towards the northwestern region, where the current active spreading center is located. Another hypothesis to explain the more youthful genesis of the CB is that the cross-basin faults do not fully propagate and instead become abandoned, leading to the development of new cross-basin faults toward the active zones connecting the bounding faults, namely the Carmen transform fault and Farallon transform fault. The significant extension rate in this part of the GC likely contributed to the abandonment of the southern and central CB sub-basins, leading to the formation of the northern CB where the current spreading center is actively accreting modern oceanic crust (Julià-Miralles et al., submitted).

The CB consists of three distinct overlapping spreading centers within the same plate-margin segment, indicating significant instability in the localization of the spreading process. These centers form grabens with increasingly advanced pull-apart geometries from south to north, suggesting strain migration in that direction. Lithospheric strength plays a crucial role in strain localization, and compositional and thermal heterogeneities in the upper mantle are likely to have significantly influenced the positioning of spreading axes. Seismic tomography conducted by Wang et al. (2009) and Di Luccio et al. (2014) revealed robust upwelling with low-shear velocity near the more stable Guaymas and Farallon spreading systems. However, these mantle anomalies are offset toward the east compared to the surface trace of these spreading systems. The distribution of applied tectonic loads along the plate margin is another factor that strongly controls strain localization.

ISSN-On line: 2444-4987

Fletcher et al. (2007) proposed that the capture of the Baja California microplate was driven by the coupling of the continental crust with the underplated oceanic lithosphere Farallon-derived microplates that became welded to the Pacific plate across the paleo East Pacific Rise west of Baja California. Therefore, tectonic loads should be most strongly applied to the lithosphere along the trailing edge of the shallowly underplated Farallon slab along the western limit of the Baja California microplate.

Conclusions

The seismic analysis of the CB reveals the acoustic basement consists of volcanic rocks, indicating the formation of a new oceanic floor within the basin. Multiple faults intersect the acoustic basement, contributing to penetrative deformation. The sedimentation process in the sub-basin system is dynamic and influenced by mass movements from sidewall fault scarps and dendritic drainage systems. These structures have accumulated significant amounts of detrital sediments.

The oceanic crust of the CB is delimited by major basin sidewall faults, alongside magmatic activity occurring along transform faults. This magmatic accretion suggests the presence of intermediate-fast-slipping transform faults, separated by a segment of intra-transform spreading center. This configuration resembles the extensional dynamics observed in the East Pacific Rise towards the mouth of the GC.

The formation of the CB initiated in the southern region, with sediment thickness gradually decreases towards the northern CB. The reactivation of the East Pacific Rise beneath the GC plays a significant role in influencing the relocation of spreading axes. Areas with thinner and fractured crust become favored during this process. As a result, sub-basins and fossil spreading centers are abandoned in the southern and central CB, while an active spreading center persists in the northern CB. Further north, near the Carmen transform fault, the development of ring faults and mud volcanoes may contribute to the future migration of a spreading center.

Acknowledgments

We thank the Schmidt Ocean Institute and the *R/V Falkor* crew for their support during expedition FK210922. Our gratitude goes to Juan Contreras, Isabela Macias and Juan Manuel Wagner for their contributions to seismic and illustration software management. We are grateful to UABC and CONAHCYT for the founding of this project. This work is contribution No. 8 from the academic team *Geología Costera UABC-CA-38*.

Financing

This work has been founded by CONAHCYT [grant number 1011828, 319430]; UABC [grant number 401/1/C/13/23].

References

Atwater, T. (1970). Implications of plate tectonics for the Cenozoic tectonic evolution of western North America. Geological Society of America Bulletin, 81(12), 3513-3536. https://doi.org/10.1130/0016-7606(1970)81[3513:IOPTFT]2.0.CO;2

Atwater, T. and Stock, J. (1998). Pacific-North America plate tectonics of the Neogene southwestern United States: an update. International Geology Review, 40(5), 375-402. https://doi.org/10.1080/00206819809465216

Balestrieri, M.L., Ferrari, L., Bonini, M., Duque-Trujillo, J., Cerca, M., Moratti, G., & Corti, G. (2017). Onshore and offshore apatite fission-track dating from the southern Gulf of California: Insights into the time-space evolution of the rifting: Tectonophysics, 719, 148-161. https://doi.org/10.1016/j.tecto.2017.05.012

Bennett, S. E., Oskin, M. E., Iriondo, A., & Kunk, M. J. (2016). Slip history of the La Cruz fault: Development of a late Miocene transform in response to increased rift obliquity in the northern Gulf of California. Tectonophysics, 693, 409-435. https://doi.org/10.1016/j.tecto.2016.06.013

ISSN-On line: 2444-4987

Bohannon, R. G., & Parsons, T. (1995). Tectonic implications of post–30 Ma Pacific and North American relative plate motions. Geological Society of America Bulletin, 107(8), 937-959. https://doi.org/10.1130/0016-7606(1995)107<0937:TIOPMP>2.3.CO;2

Bot, A., Geoffroy, L., Authemayou, C., Bellon, H., Graindorge, D., & Pik, R. (2016). Miocene detachment faulting predating EPR propagation: Southern Baja California. Tectonics, 35(5), 1153-1176. https://doi.org/10.1002/2015TC004030

Buck, W. R. (1988). Flexural rotation of normal faults. Tectonics, 7(5), 959-973. https://doi.org/10.1029/TC007i005p00959

Buck, W. R. (1993). Effect of lithospheric thickness on the formation of high-and low-angle normal faults. Geology, 21(10), 933-936. https://doi.org/10.1130/0091-7613(1993)021<0933:EOLTOT>2.3.CO;2

Bunge, H. P., & Grand, S. P. (2000). Mesozoic plate-motion history below the northeast Pacific Ocean from seismic images of the subducted Farallon slab. Nature, 405(6784), 337-340. 10.1038/35012586

Canales, J. P., Detrick, R. S., Lin, J., Collins, J. A., & Toomey, D. R. (2000). Crustal and upper mantle seismic structure beneath the rift mountains and across a nontransform offset at the Mid Atlantic Ridge (35 N). Journal of Geophysical Research: Solid Earth, 105(B2), 2699-2719. https://doi.org/10.1029/1999JB900379

Canales, J.P, Detrick, R. S., Toomey, D. R., & Wilcock, W. S. (2003). Segment-scale variations in the crustal structure of 150–300 kyr old fast spreading oceanic crust (East Pacific Rise, 8 15′ N–10 5′ N) from wide-angle seismic refraction profiles. Geophysical Journal International, 152(3), 766-794. https://doi.org/10.1046/j.1365-246X.2003.01885.x

Chopra, S., Marfurt, K.J. (2007), Seismic attributes for prospect identification and reservoir characterization. Tulsa, Oklahoma, U.S.A., Society of Exploration Geophysicists and European Association of Geoscientists and Engineers, 457 pp. https://doi.org/10.1190/1.9781560801900

Di Luccio, F., Persaud, P., Clayton, R.W. (2014). Seismic structure beneath the Gulf of California: a contribution from group velocity measurements. Geophys. J. Int. 199, 1861–1877. https://doi.org/10.1093/gji/ggu338

Dooley, T.P., & McClay, K. (1997). Analog modeling of pull-apart basins. AAPG (Am. Assoc. Pet. Geol.) Bull. 81 (11), 1804–1826. https://doi.org/10.1306/3B05C636-172A-11D7-8645000102C1865D

Escartín, J., & Lin, J. (1995). Ridge offsets, normal faulting, and gravity anomalies of slow spreading ridges. Journal of Geophysical Research: Solid Earth, 100(B4), 6163-6177. https://doi.org/10.1029/94JB03267

Ferrari, L., Orozco-Esquivel, T., Bryan, S. E., Lopez-Martinez, M., & Silva-Fragoso, A. (2018). Cenozoic magmatism and extension in western Mexico: Linking the Sierra Madre Occidental silicic large igneous province and the Comondú Group with the Gulf of California rift. Earth-Science Reviews, 183, 115-152. https://doi.org/10.1016/j.earscirev.2017.04.006

Fletcher, J. M., & Munguia, L. (2000). Active continental rifting in southern Baja California, Mexico: Implications for plate motion partitioning and the transition to seafloor spreading in the Gulf of California. Tectonics, 19(6), 1107-1123. https://doi.org/10.1029/1999TC001131

Fletcher, J. M., Kohn, B. P., Foster, D. A., & Gleadow, A. J. (2000). Heterogeneous Neogene cooling and exhumation of the Los Cabos block, southern Baja California: Evidence from fission-track thermochronology. Geology, 28(2), 107-110. https://doi.org/10.1130/0091-7613(2000)28<107:HNCAEO>2.0.CO;2

Fletcher, J. M., Grove, M., Kimbrough, D., Lovera, O., & Gehrels, G. E. (2007). Ridge-trench interactions and the Neogene tectonic evolution of the Magdalena shelf and southern Gulf of California: Insights from detrital zircon U-Pb ages from the Magdalena fan and adjacent areas. Geological Society of America Bulletin, 119(11-12), 1313-1336. https://doi.org/10.1130/B26067.1

ISSN-On line: 2444-4987

Fletcher, J. M., & Spelz, R. M. (2009). Patterns of Quaternary deformation and rupture propagation associated with an active low-angle normal fault, Laguna Salada, Mexico: Evidence of a rolling hinge? Geosphere, 5(4), 385-407. https://doi.org/10.1130/GES00206.1

Gerya, T. (2010). Dynamical instability produces transform faults at mid-ocean ridges. Science, 329(5995), 1047-1050. 10.1126/science.11913

Gregg, P. M., Lin, J., & Smith, D. K. (2006). Segmentation of transform systems on the East Pacific Rise: Implications for earthquake processes at fast-slipping oceanic transform faults. Geology, 34(4), 289-292. https://doi.org/10.1130/G22212.1

Gregg, P. M., Lin, J., Behn, M. D., & Montési, L. G. (2007). Spreading rate dependence of gravity anomalies along oceanic transform faults. Nature, 448(7150), 183-187. 10.1038/nature05962

Howell, S. M., Olive, J. A., Ito, G., Behn, M. D., Escartin, J., & Kaus, B. (2019). Seafloor expression of oceanic detachment faulting reflects gradients in mid-ocean ridge magma supply. Earth and Planetary Science Letters, 516, 176-189. https://doi.org/10.1016/j.epsl.2019.04.001

Julià-Miralles, M., Yarbuh, I., Spelz, R.M., Negrete-Aranda, R., Contreras, J., Fletcher, J.M., González-Fernández, A., Zierenberg, R., Caress, D.W. (submmited). Crustal structure and tectonic history of the Carmen Basin, southern Gulf of California: insights from high-resolution bathymetry and 2D seismic reflection profiles. Marine and Petroleum Geology. Available at SSRN: https://ssrn.com/abstract=4303241 or http://dx.doi.org/10.2139/ssrn.4303241

Kluesner, J.W., 2011. Marine geophysical study of cyclic sedimentation and shallow sill intrusion in the floor of the Central Gulf of California. UC San Diego (Ph.D. Thesis, 231 pp). https://escholarship.org/content/qt28r533bv/qt28r533bv.pdf

Kuo, B. Y., & Forsyth, D. W. (1988). Gravity anomalies of the ridge-transform system in the South Atlantic between 31 and 34.5 S: Upwelling centers and variations in crustal thickness. Marine Geophysical Researches, 10(3), 205-232. https://doi.org/10.1007/BF00310065

Lavier, L. L., Roger Buck, W., & Poliakov, A. N. (1999). Self-consistent rolling-hinge model for the evolution of large-offset low-angle normal faults. Geology, 27(12), 1127-1130. https://doi.org/10.1130/0091-7613(1999)027<1127:SCRHMF>2.3.CO;2

Lin, J., Purdy, G. M., Schouten, H., Sempere, J. C., & Zervas, C. (1990). Evidence from gravity data for focusedmagmatic accretionalong the Mid-Atlantic Ridge. Nature, 344(6267), 627-632. https://doi.org/10.1038/344627a0

Lizarralde, D., Axen, G. J., Brown, H. E., Fletcher, J. M., González-Fernández, A., Harding, A. J., ... & Umhoefer, P. J. (2007). Variation in styles of rifting in the Gulf of California. Nature, 448(7152), 466-469. https://doi.org/10.1038/nature06035

Macias-Iñiguez, I., Yarbuh, I., Spelz-Madero, R., González-Fernández, A., Fletcher, J. M., Contreras, J., ... & Guardado-France, R. (2019). Modo de extensión de la corteza y formación del Sistema Extensional de Cerralvo, sur del Golfo de California, a partir de datos de reflexión sísmica en 2D. Revista Mexicana de Ciencias Geológicas, 36(3), 334-347. https://doi.org/10.22201/cgeo.20072902e.2019.3.1352

Martín-Barajas, A., González-Escobar, M., Fletcher, J. M., Pacheco, M., Oskin, M., & Dorsey, R. (2013). Thick deltaic sedimentation and detachment faulting delay the onset of continental rupture in the Northern Gulf of California: Analysis of seismic reflection profiles. Tectonics, 32(5), 1294-1311. https://doi.org/10.1002/tect.20063

Negrete-Aranda, R., Contreras, J., & Spelz, R. M. (2013). Viscous dissipation, slab melting, and post-subduction volcanism in south-central Baja California, Mexico. Geosphere, 9(6), 1714-1728. https://doi.org/10.1130/GES00901.1

Negrete-Aranda, R., Neumann, F., Harris, R. N., Contreras, J., Zierenberg, R. A., & Caress, D. W. (2019). First Heat Flow Measurements in the Auka and JaichMaa'ja'ag vent fields Pescadero Basin, Southern Gulf of California. In AGU Fall Meeting Abstracts (Vol. 2019, pp. V13D-0187). Available at https://ui.adsabs.harvard.edu/abs/2019AGUFM.V13D0187N/abstract

Negrete-Aranda, R., Neumann, F., Contreras, J., Harris, R.N., Spelz, R.M., Zierenberg, R., Caress, D.W. (2021). Transport of Heat by Hydrothermal Circulation in a Young Rift Setting: Observations from the Auka and JaichMaa ja' ag' vent Fields in the Pescadero Basin, Southern Gulf of California. Journal of Geophysical Research: Solid Earth. https://doi.org/10.1029/2021JB022300

Nicholson, C., Sorlien, C. C., Atwater, T., Crowell, J. C., & Luyendyk, B. P. (1994). Microplate capture, rotation of the western Transverse Ranges, and initiation of the San Andreas transform as a low-angle fault system. Geology, 22(6), 491-495. https://doi.org/10.1130/0091-7613(1994)022<0491:MCROTW>2.3.CO;2

Piñero-Lajas, D. (2008). Seismic reflection and 40Ar-39Ar dating of continental basement in the western margin of Farallon basin (southern Gulf of California, Mexico). CICESE, Ensenada, Baja California, México (M.Sc. thesis in Earth Science. 155 pp). https://cicese.repositorioinstitucional.mx/jspui/handle/1007/2628. Available at https://biblioteca.cicese.mx/catalogo/tesis/ficha.php?id=17932

Ramírez-Zerpa, N., Spelz, R. M., Yarbuh, I., Negrete-Aranda, R., Contreras, J., Clague, D. A., ... & González-Fernández, A. (2022). Architecture and tectonostratigraphic evolution of the Pescadero Basin Complex, southern Gulf of California: Analysis of high-resolution bathymetry data and seismic reflection profiles. Journal of South American Earth Sciences, 103678. https://doi.org/10.1016/j.jsames.2021.103678

Sarkar, S., Moser, M., Berndt, C., Doll, M., Böttner, C., Chi, W. C., ... & Hensen, C. (2022). Thermal state of the Guaymas Basin derived from gas hydrate bottom simulating reflections and heat flow measurements. Journal of Geophysical Research: Solid Earth, 127(8), e2021JB023909. https://doi.org/10.1029/2021JB023909

Spencer, J. E., & Normark, W. R. (1979). Tosco-Abreojos fault zone: A Neogene transform plate boundary within the Pacific margin of southern Baja California, Mexico. Geology, 7(11), 554-557. https://doi.org/10.1130/0091-7613(1979)7<554:TFZANT>2.0.CO;2

Stock, J. M., & Hodges, K. V. (1989). Pre-Pliocene extension around the Gulf of California and the transfer of Baja California to the Pacific plate. Tectonics, 8(1), 99-115. https://doi.org/10.1029/TC008i001p00099

Sutherland, F.H., Kent, G.M., Harding, A.J., Umhoefer, P.J., Driscoll, N.W., Lizarralde, D., Fletcher, J.M., Axen, J.G., Holbrook, W.S., González-Fernández, A., Lonsdale, P. (2012). Middle Miocene to early Pliocene oblique extension in the southern Gulf of California. Geosphere 8 (4), 752–770. https://doi.org/10.1130/GES00770.1

Umhoefer, P. J. (2011). Why did the Southern Gulf of California rupture so rapidly?—Oblique divergence across hot, weak lithosphere along a tectonically active margin. GSA Today, 21(11), 4-10. https://doi.org/10.1130/G133A.1.

Umhoefer, P. J., Darin, M. H., Bennett, S. E., Skinner, L. A., Dorsey, R. J., & Oskin, M. E. (2018). Breaching of strike-slip faults and successive flooding of pull-apart basins to form the Gulf of California seaway from ca. 8–6 Ma. Geology, 46(8), 695-698. 10.1130/G40242.1

Umhoefer, P.J., Plattner, C., and Malservisi, R. (2020). Quantifying rates of "rifting while drifting" in the southern Gulf of California: The role of the southern Baja California microplate and its eastern boundary zone: Lithosphere, v. 12, p. 122–132. https://doi.org/10.1130/L1132.1

Wang, Y., Forsyth, D. W., & Savage, B. (2009). Convective upwelling in the mantle beneath the Gulf of California. Nature, 462(7272), 499-501. 10.1038/nature08552

ISSN-On line: 2444-4987

Wang, Y., Forsyth, D. W., Rau, C. J., Carriero, N., Schmandt, B., Gaherty, J. B., & Savage, B. (2013). Fossil slabs attached to unsubducted fragments of the Farallon plate. Proceedings of the National Academy of Sciences, 110(14), 5342-5346. https://doi.org/10.1073/pnas.1214880110

Wernicke, B., & Axen, G. J. (1988). On the role of isostasy in the evolution of normal fault systems. Geology, 16(9), 848-851. https://doi.org/10.1130/0091-7613(1988)016<0848:OTROII>2.3.CO;2

Wright, N. M., Seton, M., Williams, S. E., & Mueller, R. D. (2016). The Late Cretaceous to recent tectonic history of the Pacific Ocean basin. Earth-Science Reviews, 154, 138-173. https://doi.org/10.1016/j.earscirev.2015.11.015

Wu, J.E., McClay, K., Whitehouse, P., and Dooley, T. (2009), 4D analogue modelling of transtensional pull-apart basins: Marine and Petroleum Geology, v. 26, p. 1608–1623. https://doi.org/10.1016/j.marpetgeo.2008.06.007

Yilmaz, Ö. (2001). Seismic data analysis: Processing, inversion, and interpretation of seismic data, vol. 1, Society of Exploration Geophysicists, Tulsa, 2027 pp. https://doi.org/10.1190/1.9781560801580.fm

Zhao, D. (2004). Global tomographic images of mantle plumes and subducting slabs: insight into deep Earth dynamics. Physics of the Earth and Planetary Interiors, 146(1-2), 3-34. https://doi.org/10.1016/j.pepi.2003.07.032

ISSN-On line: 2444-4987

Article **Journal of Research and Development**
June 2023, Vol.9 No.23 29-36

Design of a two-stage air monitoring and filtration system for implementation in enclosed spaces

Diseño de un sistema para el monitoreo y filtración de aire en dos etapas para su implementación en espacios cerrados

HERNÁNDEZ-SÁNCHEZ, Uriel Alejandro†*, VÁZQUEZ-ROSAS, Sergio, CABALLERO-LÓPEZ, Emma Isabel and FLORES-SÁNCHEZ, Verónica

Universidad Tecnológica del Centro de Veracruz, Ingeniería en Mantenimiento Industrial, Av. Universidad 350, Cuitláhuac, C.P. 94910, Veracruz, México.

ID 1st Author: *Uriel Alejandro, Hernandez-Sánchez* / **ORC ID:** 0000-0003-1488-3601, **Researcher ID Thomson:** Q-2907-2018, **CVU CONAHCYT ID:** 482289

ID 1st Co-author: *Sergio, Vázquez-Rosas* / **ORC ID:** 0000-0002-3259-382X, **Researcher ID Thomson:** P-8011-2018, **CVU CONAHCYT ID:** 857794

ID 2nd Co-author: *Emma Isabel, Caballero-López* / **ORC ID:** 0000-0002-6486-9368, **Researcher ID Thomson:** ABH-3859-2020, **CVU CONAHCYT ID:** 660625

ID 3rd Co-author: *Verónica, Flores-Sánchez* / **ORC ID:** 0000-0001-7899-4592, **Researcher ID Thomson:** O-2622-2018, **CVU CONAHCYT ID:** 344279

DOI: 10.35429/JRD.2023.23.9.29.36 Received: January 30, 2023; Accepted: June 30, 2023

Abstract

The objective of this paper is to develop an air quality monitoring system implemented indoors. Our research is qualitative approach and a descriptive scope, since, the measurement of CO_2 levels will be performed from an automated system that will be monitoring this parameter and to determine whether the air quality is adequate or air recirculation is required. The study focused on the detection of carbon dioxide CO_2 over a 12-day period. The results obtained from the monitoring system show average values of 600 ppm for the dirty air sensor, while values of 488 ppm were obtained at the system output. Therefore, the performance of the system for air filtration is verified.

Air quality, CO_2 levels, Enclosed spaces monitoring, Programmable Logic Controller, Recirculation

Resumen

El presente trabajo de investigación tiene como objetivo el crear un sistema para el monitoreo y filtrado de aire en dos etapas para su implementación en interiores. La investigación se desarrolla mediante un enfoque cualitativo y un alcance descriptivo, puesto que, se realizará la medición de los niveles de CO_2 a partir de un sistema automatizado que estará monitoreando dicho parámetro y poder determinar si la calidad de aire es adecuada o se requiere de una recirculación del aire. El estudio se enfocó en la detección de dióxido de carbono CO_2, durante un periodo de 12 días. Los resultados obtenidos del sistema de monitoreo demuestran valores promedio de 600 ppm para el sensor de aire sucio, mientras que en la salida del sistema se obtuvieron valores de 488 ppm. Por consiguiente, se comprueba el funcionamiento del sistema para el filtrado de aire.

Calidad del aire, Controlador lógico programable, Monitoreo de espacios cerrados, Niveles de CO_2, Recirculación

Citation: HERNÁNDEZ-SÁNCHEZ, Uriel Alejandro, VÁZQUEZ-ROSAS, Sergio, CABALLERO-LÓPEZ, Emma Isabel and FLORES-SÁNCHEZ, Verónica. Design of a two-stage air monitoring and filtration system for implementation in enclosed spaces. Journal of Research and Development. 2023. 9-23:29-36.

† Researcher contributing as first author.

Introduction

Most of the activities performed by humans take place in enclosed spaces, such as classrooms, homes and offices, the latter being an environment that may involve health risks, either because of the nature of the work or because this space does not have optimal conditions with respect to breathing air quality, i.e. the physical, chemical and/or biological factors that interact with each other (Bian *et al*., 2018). Indoor air quality refers to air pollution inside buildings, commercial premises, airports, offices, industries, etc. The study of indoor air quality is an environmental problem; therefore, it has been posited that indoor pollution implies negative health effects (Kelly & Fussell, 2019). Measuring air quality requires tools and methods that are special for measuring the concentration level of physical and chemical properties of pollutants present indoors, another of the most widely used methods is the monitoring of suspended particles which employ filters to calculate their proportion present in the air (Braniš *et al*., 2005).

Advances in air monitoring methods have made it possible to analyse long-term pollution phenomena (Li & Bi, 2023). The parameters that determine indoor air quality are classified according to their nature as physical (such as temperature, radiation), chemical (such as organic and inorganic substances and/or compounds present in the air and/or airborne dust) or biological (moulds, spores, bacteria or mites), and the qualification of these pollutants is expanded in table 1 (Fromme *et al*., 2008). In order to carry out a correct measurement of air quality it is necessary to know the levels of chemical and biological contamination, which are provided by temperature and humidity, on the other hand, these levels are provided by sensors.

Pollutant	Type of pollutant
Organic	Volatile organic compounds (VOCs).
Inorganic	Carbon monoxide, carbon dioxide, nitrogen oxides,
Allergens	particulate matter.
Contaminants of biological origin	Fungi, moulds, dust mites, dander and pet hair.
Mixtures	Viruses, fungi, bacteria, dust mites, pet hair and dander.

Table 1 Classification of indoor containing agents
Source: Own elaboration

Air quality sensors are devices that detect and measure changes in the concentration of specific pollutants (Concas *et al*., 2021). The quality of a measurement is dictated by the basic performance of the sensor, the way the sensor is operated and the way its measurements are analysed (Anjum *et al*., 2021). There are several types of sensors, including electrochemical (EC) and optical sensors. Electrochemical sensors allow the determination of CO_2 and volatile organic compounds present in the environment in PPM concentration, based on an electrochemical semiconductor that generates an output voltage proportional to the concentration of pollutant material. A disadvantage is that the accuracy of the measurement is affected by temperature and humidity. There are several types of EC sensors, such as the MQ-7 and the MQ135. The former can measure carbon dioxide gas (CO_2), which is ideal for detecting harmful concentrations of CO_2 in the air to avoid a harmful impact on health. It can detect concentrations in the range of 20 to 2000ppm (Basford *et al*., 2020).

On the other hand, the MQ135 sensor used for air quality monitoring equipment is suitable for detecting CO_2, NH_3, benzene, NOx, smoke and alcohol. These types of gases can be harmful to health (Stavroulas *et al*., 2020). The sensor is integrated by an electronic circuit which is interfaced to a development board and has an analogue and a digital output (Dominutti *et al*., 2020). Optical sensors are the method of choice for detection due to their low cost, power requirements and fast response time. In this technique, a light source illuminates the particles, which are then measured with a photometer. For particles with diameters larger than 0.3 microns, the amount of light scattered is roughly proportional to their mass/number concentration. Particles smaller than 0.3 microns do not scatter enough light and cannot be detected by this method (Lambey & Prasad, 2021).

On the other hand, the control of temperature (both surface and air), humidity, and air quality in an indoor space generates a higher control of air pollutants. The concentration of carbon dioxide (CO_2) is a new indoor air quality check as it is a clear indicator of the performance of the air renewal system (Pichat *et al*., 2000).

ISSN-On line: 2444-4987

Several projects have been carried out to purify the air, some of which are the photocatalysis on TiO_2, which was able to test the rate of photocatalytic degradation using a laboratory photoreactor, with these data obtained it was concluded that pollutants inside a room are reduced by 43% by photocatalysis of TiO_2 (Karagulian *et al*., 2019).

On the other hand, research has been developed where transparent indoor air filters are used, these filters are composed of polymer nanofibres, the attributes obtained by this filter is that they have high filtering efficiency, logical transparency, low air resistance and light weight. This filter can prevent PM from entering the interior of the room, it can be used as a stand-alone device or incorporated with other filters such as HEPA in order to achieve a more pleasant indoor living environment (Liu *et al*., 2015). The PCO air purification technique mostly uses nano semiconductor catalysts and ultraviolet light to convert organic compounds in the air into benign and odourless constituents (Zhou *et al*., 2019).

Existing devices with applications in industry, education and government institutions have high costs, large dimensions, operational requirements and complexity of application. The implementation of such devices is limited to the geographical and temporal conditions of the areas where they are implemented. In recent years, the importance of measuring and filtering air for the prevention of diseases in people in workplaces, schools and homes has been detected.

Methodology to be developed

The present project is developed using a quantitative approach, since data will be collected for the evaluation of air quality. The scope of the research is descriptive, where the characteristics, properties and profiles of individuals or processes that can be susceptible to collection, measurement, evaluation and information of the variables examined are examined (Hernández Sampieri *et al*., 2014).

Therefore, the research work is carried out through a descriptive scope, since, exposure levels of various pollutants will be collected to establish alert levels for the prevention of harmful effects on health.

Figure 1 describes the 3 methodological stages applied to the project. In the first stage, the relevant calculations were carried out to determine the volume of the space, air changes per hour, CO_2 concentration and to estimate the clean air in the study area. Then we proceeded to design the device, starting with the selection of a free platform to facilitate the management of the information, then the response algorithm was developed, then the components of the device were integrated. Finally, a pilot test was carried out to check the performance and functionality of the device.

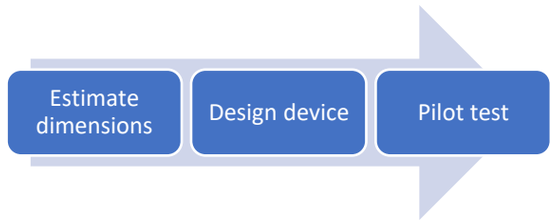

Figure 1 Methodology applied
Source: Own elaboration

Design of the device

The first step to develop the device is to select the platform that allows the development of the research work, therefore, the different platforms that will facilitate the transmission of information generated by the sensor were investigated. A free software platform was selected, which can be replicated as long as the equipment is available to carry out the monitoring. Then the elements that will integrate the air quality monitoring system were selected, which are shown in figure 2; two MQ-135 sensors for air quality control, an air extractor, UV-c lamp and a Logo 8.3 programmable logic control (PLC) that includes an LCD screen for data visualisation, power and ethernet ports for connection to the cloud.

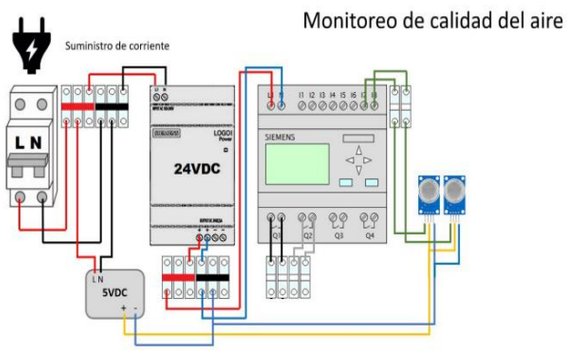

Figure 2 Wiring schematic and monitoring system components
Source: Own elaboration

ISSN-On line: 2444-4987

In order for the system to process the signals generated by the MQ-135 sensor, the flow diagram of the air quality monitoring system is shown (figure 3); The sensor is in continuous operation, therefore, it will detect measurements that exceed 500 ppm, when the levels exceed the concentration limit, a signal will be sent to activate an air extractor and an ultraviolet light lamp (UV-c), the extracted air will pass through a chamber in which a HEPA filter and an activated carbon filter are installed and ends up passing through the UV-c lamp. A second MQ-135 sensor is located at the air outlet to analyse whether the air being processed for filtration is below 500 ppm. Finally, when the sensor detects readings below 500 ppm a signal will be sent to determine the filtration system, however, the first sensor will continue to take real-time readings of the air quality levels.

The next stage is the development of the block diagram shown in figure 4. This programming code has 3 inputs, two analogue (AI1 and AI2) and one digital (I1). The input (AI1) captures the CO_2 concentration in the polluted environment.

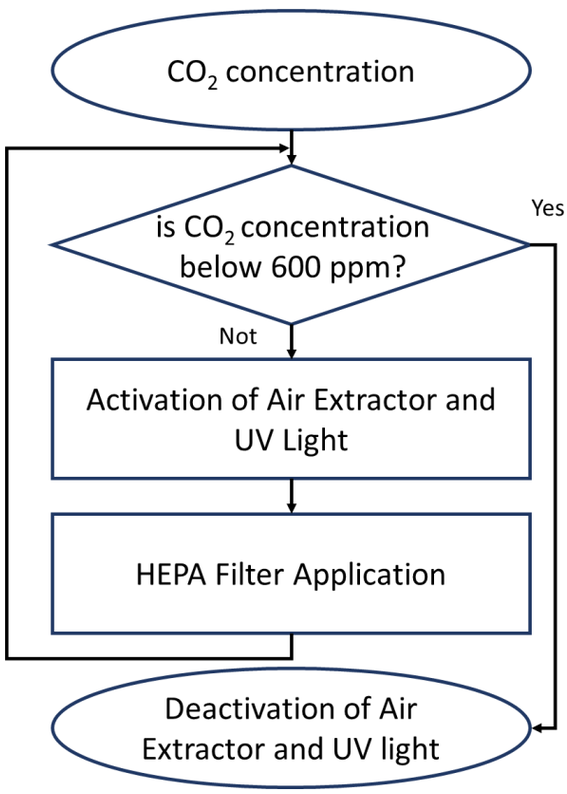

Figure 3 Algorithm flowchart
Source: Own elaboration

The signal is then processed in an arithmetic operation block to determine the carbon dioxide concentration values in ppm (parts per million). An analogue threshold value switch activates the outputs Q1 and Q2 (extractor and UV light) when the values are equal to or greater than 550 ppm. If values below 500 ppm are registered, the actuators (extractor and UV light) will remain off.

UV light) will remain switched off. The input (AI2) is connected to the filtered ambient sensor, which will perform the same signal conditioning process except that this input will only register carbon dioxide concentration values. The digital input is a push button that will force the system on and off the outputs.

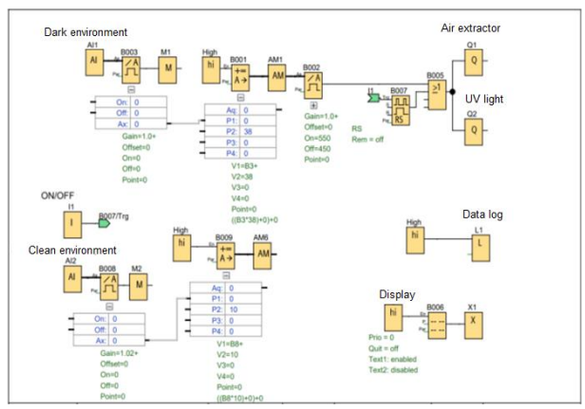

Figure 4 *Block diagram of the system*
Source: Own elaboration

The design of the air purification cabin was made using CAD SolidWorks 2018 software where: different projection views were developed, a breakdown of the components for assembly is observed. Figure 5 shows the arrangement of the purification filters used in the design, with a pre-filter of filter cloth (made with fiberglass mesh), a HEPA filter, an activated carbon filter and a UV sterilization system.

ISSN-On line: 2444-4987

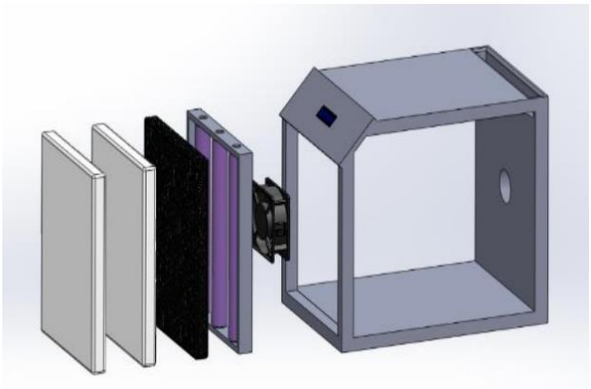

Figure 5 Exploded view of the system
Source: Own elaboration

Finally, a device was developed to place the MQ-135 sensors and the air filtration system, which can be seen in figure 6. The design of the filtration system starts with the extraction of the air inside the equipment to begin the filtering process. As a first stage, a fabric pre-filter is placed to remove dust particles, dirt and most of the pollutants found in the air. Afterwards, the air passes through an activated carbon filter that will remove odors, toxic solvents and chemical vapors and, if necessary, will retain cigarette smoke. Next, a HEPA H13 filter of 0.01µm to 0.3µm will reduce the presence of allergens by 99.95%; furthermore, the implementation of the filter is essential to trap most microscopic particles such as viruses and bacteria including SARS-COV2. Finally, the air will undergo UV sterilization to kill or inactivate viruses, molds, bacteria and micro-organisms that have not been filtered out in the previous process by destroying their genetic material (DNA or RNA). And thus, return clean air free of microorganisms to the room where the purifier is located.

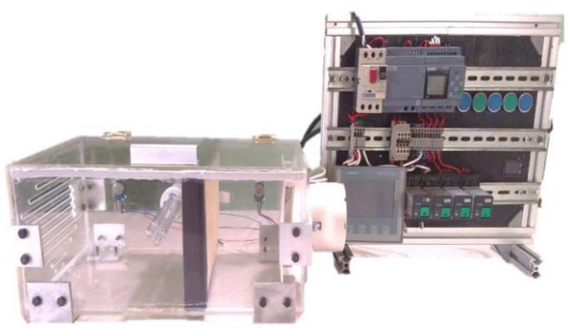

Figure 6 Measurement and filtration system
Source: Own elaboration

Results

In this section, the results of the proper functioning of the sensors, the processing and collection of information will be demonstrated. Subsequently, the behavior of the data generated by the system will be analyzed.

The dimensions of the equipment were determined based on the size of the classrooms, where V represents the volume of the classroom defined in Equation 1, where l is length, b is width and h is height, with a resulting volume of $30m^2$.

$$V = l * b * h = 2.5m * 4m * 3m = 30m^2 \quad (1)$$

According to DIN 1946, the recommended number of air changes per hour is 5-7 for the tertiary sector (classrooms), which when multiplied by the volume, gives the clean air flow specified in Equation 2, where Q is clean air flow, V is classroom volume and R/H is air changes per hour.

$$\mathrm{Q} = \mathrm{V} * \mathrm{RH} = 30m^3 * 5\mathrm{hr} = 150m^3/hr \quad (2)$$

The ANSI/AHAM AC-1 standard is consistent with the method for verifying the performance of electric air purifiers in enclosed spaces. In this standard, the clean air flow rate is expressed in CADR (Clean Air Delivery Rate) and its unit is m3/h. Therefore, the exhaust fan must maintain a CADR of 150 m3/h. Also in the CSIC guide for classroom ventilation, it is recommended to include the number of people in the room, by means of Equation 3, where ACH is the air change per hour and is obtained by multiplying the volume of air contained in the purifier multiplied by the number of people and the adjustment constant, over the volume of the room.

$$ACH = \frac{(14liters)(25\ people\ )\ (3600s)\ (0.001m^3)}{30m^3} = 42 \quad (3)$$

Comparing the data obtained, it is established that a classroom with a volume of $30m^3$ requires a flow rate of $150m^3$/hr in a full day of classes (5hr), so that the activation of the purifier is adjusted to 42 renewals per hour. Figure 7 shows the behavior of the equipment, under controlled conditions of 24 students and one teacher.

ISSN-On line: 2444-4987

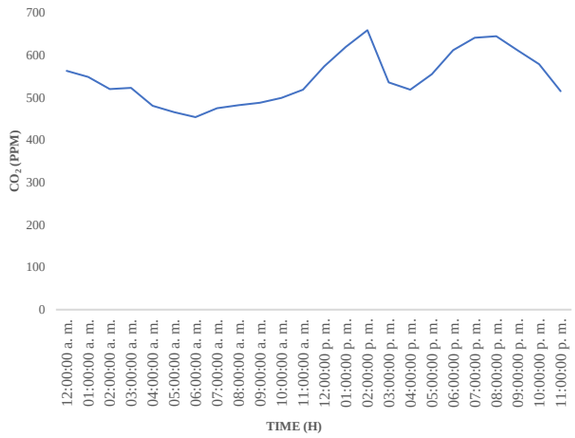

Figure 7 CO_2 behavior in an evening class day (5hr), $30m^3$ classroom, 42 renewals/hr.
Source: Own elaboration

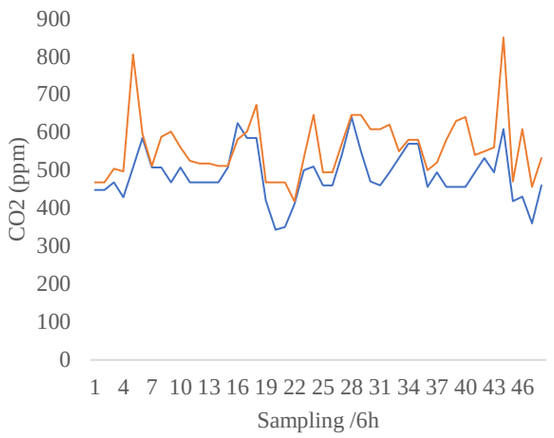

Figure 8 CO_2 behavior over 12 days, 30m3 classroom, 42 renewals/hr.
Source: Own elaboration

Figure 8 shows the behaviour of CO_2 over a period of 288 hours of analysis to generate precision in the data collected. Averages of 600 ppm were obtained in the polluted environment sensor. On the other hand, the clean air sensor obtained values between 343 ppm and 608 ppm. Consequently, it is possible to demonstrate that the device maintains the minimum values of CO_2 concentration in closed spaces, which are recommended not to exceed 800 ppm and do not represent a health risk.

One of the characteristics of carbon dioxide is that it is a gas that does not harm human health; however, in high concentrations it can have repercussions on people's integrity. For example, it can cause asphyxiation due to the reduction of oxygen in space. Due to the health contingency caused by the SARS-CoV-2 virus, which is transmitted through the air under certain conditions in enclosed spaces. Measuring carbon dioxide helps to reduce pollutants by monitoring air quality. Systems such as the one designed allow the accumulation of CO_2 in indoor spaces to be quantified and help to improve quality by activating an air renewal and purification system to achieve acceptable levels of this pollutant.

The values obtained during the 12 days of evaluation are within the parameters specified by the Occupational Safety and Health Administration (OSHA), which specifies reference values for 8 hours of CO_2, the indicator is 5000 ppm. To validate the effectiveness of the system, it is planned to implement it in certain areas in the future. In addition, sensors for the measurement of PM_{10} and $PM_{2.5}$ particulate matter will be implemented. Another aspect that will improve the monitoring of these parameters is the enabling of IoT for the visualization of results in real time in places with internet access.

Conclusions

A system was designed to assess indoor air quality based on the detection of indoor carbon dioxide CO_2. The system only allows real-time visualization and downloading of measurements collected during the period it is activated. The results show average values of 600 ppm for dirty air conditions and 488 ppm for filtered air. The results show that when CO_2 values higher than 550 ppm are detected, the filtering system is activated, then, at the air outlet, values in the range of 300 ppm lower than the inlet value are provided. Therefore, the creation of a system for monitoring and filtering air in two stages for indoor implementation was achieved, achieving its function and demonstrating that the objective of the research is fulfilled.

ISSN-On line: 2444-4987

It is important to carry out studies for the evaluation of the exposure times to which people are exposed to indoor and outdoor air pollutants, since this makes it possible to identify the relationship between the concentration of the pollutants in the air and the concentration of the pollutants in the air.

The existence of studies that focus on the concentration of pollutants and the possible effects on people's health is important. The existence of studies that focus on the air filtering process is vital to be able to prevent and predict the risks to which the population is exposed and, consequently, to be able to establish the necessary regulations for indoor air quality according to the conditions of the country.

To conclude, the concentration of carbon dioxide (CO_2) increases if a large number of people are gathered inside a room, which leads to a decrease in air quality and therefore, as there are more people in the same place, the spread of viruses and bacteria increases. And a cause of COVID-19 contagion is that there is an agglomeration of people, which is why it is necessary to have equipment in charge of purifying the air, mitigating the contagion not only of COVID but of all diseases derived from viruses and bacteria.

References

Anjum, M. S., Ali, S. M., Imad-ud-din, M., Subhani, M. A., Anwar, M. N., Nizami, A. S., Ashraf, U., & Khokhar, M. F. (2021). An Emerged Challenge of Air Pollution and Ever-Increasing Particulate Matter in Pakistan; A Critical Review. *Journal of Hazardous Materials*, *402*. https://doi.org/10.1016/j.jhazmat.2020.123943

Basford, P. J., Bulot, F. M. J., Apetroaie-Cristea, M., Cox, S. J., & Ossont, S. J. J. (2020). LoRaWan for smart city IoT deployments: A long term evaluation. *Sensors (Switzerland)*, *20*(3). https://doi.org/10.3390/s20030648

Bian, Y., Wang, R., Wang, S., Yao, C., Ren, W., Chen, C., & Zhang, L. (2018). Metal-organic framework-based nanofiber filters for effective indoor air quality control. *Journal of Materials Chemistry A*, *6*(32). https://doi.org/10.1039/c8ta04539a

Braniš, M., Řezáčová, P., & Domasová, M. (2005). The effect of outdoor air and indoor human activity on mass concentrations of PM10, PM2.5, and PM1 in a classroom. *Environmental Research*, *99*(2). https://doi.org/10.1016/j.envres.2004.12.001

Concas, F., Mineraud, J., Lagerspetz, E., Varjonen, S., Liu, X., Puolamäki, K., Nurmi, P., & Tarkoma, S. (2021). Low-Cost Outdoor Air Quality Monitoring and Sensor Calibration. In *ACM Transactions on Sensor Networks* (Vol. 17, Issue 2). https://doi.org/10.1145/3446005

Dominutti, P., Nogueira, T., Fornaro, A., & Borbon, A. (2020). One decade of VOCs measurements in São Paulo megacity: Composition, variability, and emission evaluation in a biofuel usage context. *Science of the Total Environment*, *738*. https://doi.org/10.1016/j.scitotenv.2020.139790

Fromme, H., Diemer, J., Dietrich, S., Cyrys, J., Heinrich, J., Lang, W., Kiranoglu, M., & Twardella, D. (2008). Chemical and morphological properties of particulate matter (PM10, PM2.5) in school classrooms and outdoor air. *Atmospheric Environment*, *42*(27). https://doi.org/10.1016/j.atmosenv.2008.04.047

Hernandez Sampieri, R., Fernandez Collado, C., & Baptista, M. del P. (2014). Metodologia de la Investigacion (6ta edicion). In *Mc Graw Hill*.

Karagulian, F., Barbiere, M., Kotsev, A., Spinelle, L., Gerboles, M., Lagler, F., Redon, N., Crunaire, S., & Borowiak, A. (2019). Review of the performance of low-cost sensors for air quality monitoring. In *Atmosphere* (Vol. 10, Issue 9). https://doi.org/10.3390/atmos10090506

Kelly, F. J., & Fussell, J. C. (2019). Improving indoor air quality, health and performance within environments where people live, travel, learn and work. In *Atmospheric Environment* (Vol. 200). https://doi.org/10.1016/j.atmosenv.2018.11.058

Lambey, V., & Prasad, A. D. (2021). A Review on Air Quality Measurement Using an Unmanned Aerial Vehicle. In *Water, Air, and Soil Pollution* (Vol. 232, Issue 3). https://doi.org/10.1007/s11270-020-04973-5

ISSN-On line: 2444-4987

Li, J., & Bi, C. (2023). Visual analysis of air pollution spatio-temporal patterns. *Visual Computer*, *39*(8). https://doi.org/10.1007/s00371-023-02961-4

Liu, C., Hsu, P. C., Lee, H. W., Ye, M., Zheng, G., Liu, N., Li, W., & Cui, Y. (2015). Transparent air filter for high-efficiency PM 2.5 capture. *Nature Communications*, *6*. https://doi.org/10.1038/ncomms7205

Pichat, P., Disdier, J., Hoang-Van, C., Mas, D., Goutailler, G., & Gaysse, C. (2000). Purification/deodorization of indoor air and gaseous effluents by TiO2 photocatalysis. *Catalysis Today*, *63*(2–4). https://doi.org/10.1016/S0920-5861(00)00480-6

Stavroulas, I., Grivas, G., Michalopoulos, P., Liakakou, E., Bougiatioti, A., Kalkavouras, P., Fameli, K. M., Hatzianastassiou, N., Mihalopoulos, N., & Gerasopoulos, E. (2020). Field evaluation of low-cost PM sensors (Purple Air PA-II) Under variable urban air quality conditions, in Greece. *Atmosphere*, *11*(9). https://doi.org/10.3390/atmos11090926

Zhou, Y., Chang, F. J., Chang, L. C., Kao, I. F., & Wang, Y. S. (2019). Explore a deep learning multi-output neural network for regional multi-step-ahead air quality forecasts. *Journal of Cleaner Production*, *209*. https://doi.org/10.1016/j.jclepro.2018.10.243

ISSN-On line: 2444-4987

[Title in Times New Roman and Bold No. 14 in English and Spanish]

Surname (IN UPPERCASE), Name 1st Author†*, Surname (IN UPPERCASE), Name 1st Coauthor, Surname (IN UPPERCASE), Name 2nd Coauthor and Surname (IN UPPERCASE), Name 3rd Coauthor

Institutional Affiliation of Author including Dependency (No.10 Times New Roman and Italic)

International Identification of Science - Technology and Innovation

ID 1st Author: (ORC ID - Researcher ID Thomson, arXiv Author ID - PubMed Author ID - Open ID) and CVU 1st author: (Scholar-PNPC or SNI-CONAHCYT) (No.10 Times New Roman)

ID 1st Coauthor: (ORC ID - Researcher ID Thomson, arXiv Author ID - PubMed Author ID - Open ID) and CVU 1st coauthor: (Scholar or SNI) (No.10 Times New Roman)

ID 2nd Coauthor: (ORC ID - Researcher ID Thomson, arXiv Author ID - PubMed Author ID - Open ID) and CVU 2nd coauthor: (Scholar or SNI) (No.10 Times New Roman)

ID 3rd Coauthor: (ORC ID - Researcher ID Thomson, arXiv Author ID - PubMed Author ID - Open ID) and CVU 3rd coauthor: (Scholar or SNI) (No.10 Times New Roman)

(Report Submission Date: Month, Day, and Year); Accepted (Insert date of Acceptance: Use Only ECORFAN)

Abstract (In English, 150-200 words)

Objectives
Methodology
Contribution

Keywords (In English)

Indicate 3 keywords in Times New Roman and Bold No. 10

Abstract (In Spanish, 150-200 words)

Objectives
Methodology
Contribution

Keywords (In Spanish)

Indicate 3 keywords in Times New Roman and Bold No. 10

Citation: Surname (IN UPPERCASE), Name 1st Author, Surname (IN UPPERCASE), Name 1st Coauthor, Surname (IN UPPERCASE), Name 2nd Coauthor and Surname (IN UPPERCASE), Name 3rd Coauthor. Paper Title. Journal of Research and Development. Year 1-1: 1-11 [Times New Roman No.10]

* Correspondence to Author (example@example.org)
† Researcher contributing as first author.

Journal of Research and Development
Month, Year Vol.1 No.1 1-15-[Using ECORFAN]

Introduction

Text in Times New Roman No.12, single space.

General explanation of the subject and explain why it is important.

What is your added value with respect to other techniques?

Clearly focus each of its features

Clearly explain the problem to be solved and the central hypothesis.

Explanation of sections Article.

Development of headings and subheadings of the article with subsequent numbers

[Title No.12 in Times New Roman, single spaced and bold]

Products in development No.12 Times New Roman, single spaced

Editable

In the article content any graphic, table and figure should be editable formats that can change size, type and number of letter, for the purposes of edition, these must be high quality, not pixelated and should be noticeable even reducing image scale.

[Indicating the title at the bottom with No.10 and Times New Roman Bold]

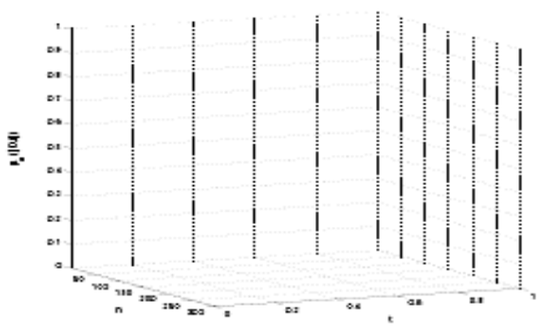

Graphic 1 Title and *Source (in italics)*

Should not be images-everything must be editable.

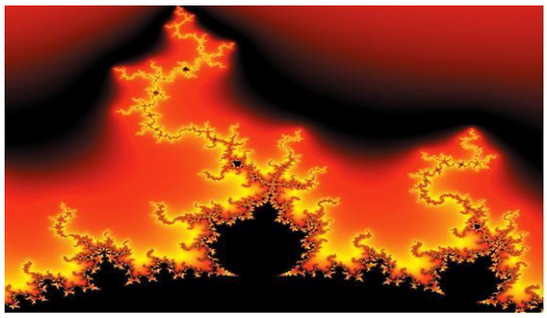

Figure 1 Title and *Source (in italics)*

Should not be images-everything must be editable.

Table 1 Title and *Source (in italics)*

Should not be images-everything must be editable.

For the use of equations, noted as follows:

$$Y_{ij} = \alpha + \sum^{r} \quad \beta_h X_{hij}$$

Must be editable and number aligned on the right side.

Methodology

Develop give the meaning of the variables in linear writing and important is the comparison of the used criteria.

Results

The results shall be by section of the article.

Annexes

Tables and adequate sources

Thanks

Indicate if they were financed by any institution, University or company.

Conclusions

Explain clearly the results and possibilities of improvement.

ISSN 2444-4987

References

Use APA system. Should not be numbered, nor with bullets, however if necessary numbering will be because reference or mention is made somewhere in the Article.

Use Roman Alphabet, all references you have used must be in the Roman Alphabet, even if you have quoted an Article, book in any of the official languages of the United Nations (English, French, German, Chinese, Russian, Portuguese, Italian, Spanish, Arabic), you must write the reference in Roman script and not in any of the official languages.

Technical Specifications

Each article must submit your dates into a Word document (.docx):

Journal Name
Article title
Abstract
Keywords
Article sections, for example:

1. Introduction
2. Description of the method
3. Analysis from the regression demand curve
4. Results
5. Thanks
6. Conclusions
7. References

Author Name (s)
Email Correspondence to Author
References

Intellectual Property Requirements for editing:

- Authentic Signature in Color of Originality Format Author and Coauthors.

- Authentic Signature in Color of the Acceptance Format of Author and Coauthors.

- Authentic Signature in blue Color of the Conflict of Interest Format of Author and Co-authors.

Reservation to Editorial Policy

Journal of Research and Development reserves the right to make editorial changes required to adapt the Articles to the Editorial Policy of the Journal. Once the Article is accepted in its final version, the Journal will send the author the proofs for review. ECORFAN® will only accept the correction of errata and errors or omissions arising from the editing process of the Journal, reserving in full the copyrights and content dissemination. No deletions, substitutions or additions that alter the formation of the Article will be accepted.

Code of Ethics - Good Practices and Declaration of Solution to Editorial Conflicts

Declaration of Originality and unpublished character of the Article, of Authors, on the obtaining of data and interpretation of results, Acknowledgments, Conflict of interests, Assignment of rights and Distribution

The ECORFAN-Mexico, S.C. Management claims to Authors of Articles that its content must be original, unpublished and of Scientific, Technological and Innovation content to be submitted for evaluation.

The Authors signing the Article must be the same that have contributed to its conception, realization and development, as well as obtaining the data, interpreting the results, drafting and reviewing it. The Corresponding Author of the proposed Article will request the form that follows.

Article title:

– The sending of an Article to Journal of Research and Development emanates the commitment of the author not to submit it simultaneously to the consideration of other series publications for it must complement the Format of Originality for its Article, unless it is rejected by the Arbitration Committee, it may be withdrawn.

– None of the data presented in this article has been plagiarized or invented. The original data are clearly distinguished from those already published. And it is known of the test in PLAGSCAN if a level of plagiarism is detected Positive will not proceed to arbitrate.

– References are cited on which the information contained in the Article is based, as well as theories and data from other previously published Articles.

– The authors sign the Format of Authorization for their Article to be disseminated by means that ECORFAN-Mexico, S.C. In its Holding Spain considers pertinent for disclosure and diffusion of its Article its Rights of Work.

– Consent has been obtained from those who have contributed unpublished data obtained through verbal or written communication, and such communication and Authorship are adequately identified.

– The Author and Co-Authors who sign this work have participated in its planning, design and execution, as well as in the interpretation of the results. They also critically reviewed the paper, approved its final version and agreed with its publication.

– No signature responsible for the work has been omitted and the criteria of Scientific Authorization are satisfied.

– The results of this Article have been interpreted objectively. Any results contrary to the point of view of those who sign are exposed and discussed in the Article.

Copyright and Access

The publication of this Article supposes the transfer of the copyright to ECORFAN-Mexico, S.C. in its Holding Spain for its Journal of Research and Development, which reserves the right to distribute on the Web the published version of the Article and the making available of the Article in This format supposes for its Authors the fulfilment of what is established in the Law of Science and Technology of the United Mexican States, regarding the obligation to allow access to the results of Scientific Research.

Article Title:

Name and Surnames of the Contact Author and the Coauthors	Signature
1.	
2.	
3.	
4.	

Principles of Ethics and Declaration of Solution to Editorial Conflicts

Editor Responsibilities

The Publisher undertakes to guarantee the confidentiality of the evaluation process, it may not disclose to the Arbitrators the identity of the Authors, nor may it reveal the identity of the Arbitrators at any time.

The Editor assumes the responsibility to properly inform the Author of the stage of the editorial process in which the text is sent, as well as the resolutions of Double-Blind Review.

The Editor should evaluate manuscripts and their intellectual content without distinction of race, gender, sexual orientation, religious beliefs, ethnicity, nationality, or the political philosophy of the Authors.

The Editor and his editing team of ECORFAN® Holdings will not disclose any information about Articles submitted to anyone other than the corresponding Author.

The Editor should make fair and impartial decisions and ensure a fair Double-Blind Review.

Responsibilities of the Editorial Board

The description of the peer review processes is made known by the Editorial Board in order that the Authors know what the evaluation criteria are and will always be willing to justify any controversy in the evaluation process. In case of Plagiarism Detection to the Article the Committee notifies the Authors for Violation to the Right of Scientific, Technological and Innovation Authorization.

Responsibilities of the Arbitration Committee

The Arbitrators undertake to notify about any unethical conduct by the Authors and to indicate all the information that may be reason to reject the publication of the Articles. In addition, they must undertake to keep confidential information related to the Articles they evaluate.

Any manuscript received for your arbitration must be treated as confidential, should not be displayed or discussed with other experts, except with the permission of the Editor.

The Arbitrators must be conducted objectively, any personal criticism of the Author is inappropriate.

The Arbitrators must express their points of view with clarity and with valid arguments that contribute to the Scientific, Technological and Innovation of the Author.

The Arbitrators should not evaluate manuscripts in which they have conflicts of interest and have been notified to the Editor before submitting the Article for Double-Blind Review.

Responsibilities of the Authors

Authors must guarantee that their articles are the product of their original work and that the data has been obtained ethically.

Authors must ensure that they have not been previously published or that they are not considered in another serial publication.

Authors must strictly follow the rules for the publication of Defined Articles by the Editorial Board.

The authors have requested that the text in all its forms be an unethical editorial behavior and is unacceptable, consequently, any manuscript that incurs in plagiarism is eliminated and not considered for publication.

Authors should cite publications that have been influential in the nature of the Article submitted to arbitration.

Information services

Indexation - Bases and Repositories

LATINDEX (Scientific Journals of Latin America, Spain and Portugal)
EBSCO (Research Database - EBSCO Industries)
RESEARCH GATE (Germany)
GOOGLE SCHOLAR (Citation indices-Google)
REDIB (Ibero-American Network of Innovation and Scientific Knowledge- CSIC)
MENDELEY (Bibliographic References Manager)

Publishing Services

Citation and Index Identification H
Management of Originality Format and Authorization
Testing Article with PLAGSCAN
Article Evaluation
Certificate of Double-Blind Review
Article Edition
Web layout
Indexing and Repository
ArticleTranslation
Article Publication
Certificate of Article
Service Billing

Editorial Policy and Management

38 Matacerquillas, CP-28411. Moralzarzal –Madrid-España. Phones: +52 1 55 6159 2296, +52 1 55 1260 0355, +52 1 55 6034 9181; Email: contact@ecorfan.org www.ecorfan.org

Journal of Research and Development

2444 4987
ISSN 2444 - 4987